Androgen receptor imprints satellite cells stemness and preserves their reservoir for lifelong regeneration and optimal repair

Joe G. Rizk[1*], Kamar C. Ghaibour[1*], Sirine Souali-Crespo[1], Aurore Bilger[1], Emilia Calvano[1], Hugues Jacobs[1], Nadia Messaddeq[1], Qingshuang Cai[1], Erwan Grangirard[1], Rajesh Sahu[1], Arnaud Ferry[2], Gianni Zanardelli[1], Nacho Molina[1], Coralie Fontaine[3], Jean-François Arnal[3], Daniel Metzger[1], Delphine Duteil[1#]

[1] Université de Strasbourg, CNRS, Inserm, IGBMC UMR 7104- UMR-S 1258, F-67400 Illkirch, France

[2] Centre de Recherche en Myologie, UMRS974-Sorbonne Université-INSERM U974-Association Institut de Myologie, France.

[3] Institut National de la Santé et de la Recherche Médicale (INSERM), U1297, Institut des Maladies Métaboliques et Cardiovasculaires (I2MC), Université Toulouse III Paul Sabatier, CHU Rangueil (University Hospital) de Toulouse, F-31432 Toulouse, France

[#] Author to whom correspondence should be addressed at duteild@igbmc.fr.

[*] These authors equally contributed to this work.

SUMMARY

Skeletal muscle stem cells (MuSC) are the guardians of muscle regeneration, sustaining tissue integrity through a delicate balance of quiescence, activation, and lineage commitment. While numerous molecular cues have been implicated in regulating these processes, the influence of androgen receptor (AR) signaling, an essential hormonal pathway for male muscle physiology, has remained largely unexplored. Here, we show that AR expression defines quiescent MuSC and acts as a safeguard of their dormancy. Integrated multi-omic analyses reveal a redistribution of AR binding from quiescence-maintenance loci to regulatory elements driving activation and metabolic reprogramming during repair. Loss of AR in young adult mice disrupts this balance, precipitating premature cell-cycle entry, skewed division modalities, depletion of the stem cell reservoir, and destabilization of the niche. These defects converge with hallmarks of aging-associated androgen decline, while androgen supplementation restores regenerative competence. Together, our findings establish AR signaling as a pivotal determinant of MuSC fate and a cornerstone of skeletal muscle homeostasis.

KEY WORDS

Satellite Cells, Androgen Receptor, Androgens, Skeletal Muscle, Regeneration, Ageing, Symmetric differentiation

35 **INTRODUCTION**

36 Skeletal muscles exhibit a remarkable regeneration capacity upon injury, resulting from the fusion of
37 newly formed myocytes to generate myofibers that replace the damaged ones. This process is initiated
38 by myofiber degeneration, causing inflammatory cell infiltration followed by the activation of satellite
39 cells, which are the muscle stem cells (MuSC) [1]. In the intact muscle, MuSC reside in a quiescent state
40 within a specialized niche between the myofiber sarcolemma and the basal lamina [2, 3]. They are
41 defined by the expression of the myogenic transcription factor paired box 7 (*Pax7*), a key marker of
42 their identity and function [4].

43 Upon muscle injury, MuSC exhibit a dual capacity. They can either self-renew to replenish the stem
44 cell pool and preserve long-term regenerative competence, or enter a proliferative phase followed by
45 activation of the myogenic differentiation program, culminating in fusion and formation of new
46 myofibers [5, 6]. These key myogenic features, are intrinsically dependent on MuSC microenvironment,
47 comprising immune and stromal cells. This microenvironment is tightly regulated by interactions with
48 extracellular matrix components, inter-cell signaling and paracrine or endocrine stimuli [7-9]. With age,
49 skeletal muscle regenerative capacities progressively decline, which has been recently attributed to a
50 reduction in MuSC number and function [10-12]. These processes are thought to be exacerbated by
51 hormonal changes, including decrease in circulating androgens [13-15].

52 Androgens are steroid hormones mainly produced by male gonads. They play a crucial role in
53 modulating muscle homeostasis and MuSC fate, both during postnatal development and at adult
54 stages [16, 17]. In young adult mice, androgens promote MuSC quiescence through a Notch-dependent
55 pathway [18], and influence their activation, proliferation, and differentiation [18-20]. In addition, androgen
56 supplementation increases MuSC numbers in both animal models and humans [21]. Oppositely,
57 castration-induced androgen deprivation in rodents leads to perturbed MuSC homeostasis [22].
58 Androgens exert their effects through the androgen receptor (AR), a ligand-activated transcription
59 factor and member of the nuclear receptor superfamily, which upon ligand binding translocates to the
60 nucleus and binds specific DNA sequences known as androgen response elements (AREs), to regulate
61 target genes expression [23-25]. We previously showed that AR in myofibers is instrumental for the
62 musculoskeletal system by controlling gene networks required for structural and metabolic demands
63 [25, 26]. Nevertheless, the role of androgens *via* AR in MuSC during muscle regeneration, the broader
64 consequences of androgen-dependent decline on the regenerative machinery, the underlying
65 molecular mechanisms, and its potential causal link to age-associated muscle degeneration remain to
66 be fully elucidated.

67 By integrating genome-wide profiling and histological analysis, with the study of an inducible MuSC-
68 specific AR knockout mouse model and stem-like myogenic cell lines, we delineate the molecular

69 mechanisms through which androgens *via* their receptor regulate MuSC regenerative functions. Our
70 findings highlight the pivotal role of MuSC-AR in muscle repair, identifying AR-dependent stem cell
71 profiles and supportive MuSC subtypes involved in postnatal myogenesis. We further reveal that AR
72 orchestrates stemness transitions by sequential chromatin repositioning following injury, thereby
73 controlling gene networks governing MuSC self-renewal, proliferation, and differentiation.
74 Additionally, we demonstrate that androgen signaling contributes to the age-related decline in muscle
75 healing capacities, and validate the translational relevance of murine findings in human myoblasts.

76 **RESULTS**

77 **AR deficiency in MuSC in young individuals compromises regenerative capacity and alters metabolic**
78 **and structural transcriptional programs in skeletal muscle**

79 To dissect the age-dependent role of AR signaling within MuSC, we generated mice with a conditional
80 AR deletion in this cell lineage (hereafter $AR^{(i)sat-/Y}$ mice). Nine-week-old mice harboring floxed *Ar*
81 alleles and expressing the *Pax7*-$CreER^{T2}$ transgene were treated with tamoxifen (TAM) for 5 days,
82 enabling selective deletion of *Ar* in MuSC (Figures S1A-S1D). TAM-treated littermates lacking the *Pax7*-
83 $CreER^{T2}$ transgene served as controls. To evaluate the functional consequences of AR ablation on
84 skeletal muscle regenerative capacities, we subjected young (3-month-old) control and $AR^{(i)sat-/Y}$ mice
85 to acute Tibialis Anterior (TA) muscle injury *via* cardiotoxin (CTX) injection one month after gene
86 ablation, and assessed histological features of repair at 5-, 7-, 14-, 28- and 42-days post-injury (dpi).
87 While no gross phenotypical abnormalities were noticed in the absence of injury (Figures S1E-S1G), At
88 5 dpi, a timepoint at which MuSC activation and early differentiation culminate [27], both genotypes
89 showed similar hallmarks of effective regeneration, including centronucleated fibers, necrosis, and
90 immune cell infiltration (Figure S1H). However, at 7 dpi, $AR^{(i)sat-/Y}$ mice exhibited regenerative defects,
91 including persistent inflammation, and aberrant fiber morphology that persisted until 42 dpi, that
92 were not due to the $CreER^{T2}$ knock-in (Figures 1A and S1H). Ultrastructural analyses performed at 7
93 dpi, a timepoint at which mononuclear cells fuse in order to form myosyncytia and primary
94 regenerative outcomes are captured [28], revealed that $AR^{(i)sat-/Y}$ muscles displayed disorganized
95 sarcomeres, with misaligned triads characterized by dilated T-tubules, disrupted Z-lines, and poorly
96 defined or absent M-lines (Figure 1B). These structural muscle defects correlated with a significant
97 reduction in myofiber cross-sectional area (Figure 1C), which translated into a significant reduction in
98 contractile force at 28 dpi (Figure 1D). Muscle dysfunction was accompanied by a marked reduction
99 in the MuSC pool at 7 dpi (Figures 1E and 1F), which persisted at 28 dpi (Figures S1I and S1J), showing
100 that loss of AR in MuSC severely impairs regenerative capacity in young male mice.

101 To elucidate AR transcriptional landscape, we conducted bulk RNA sequencing (RNA-seq) on TA
102 muscles harvested at 7 dpi from young $AR^{(i)sat-/Y}$ and control mice. Our analysis revealed a differential
103 expression of 3,586 genes, comprising 2,045 downregulated and 1,541 upregulated genes in AR-
104 deficient mice (Figures 1G and S1K). Pathway analyses of the downregulated genes highlighted a
105 strong association with biological processes involved in actin cytoskeleton organization, focal
106 adhesion, and developmental signaling cascades such as the PI3K-Akt pathway (Figure 1H). Strikingly,
107 the expression of key myogenic regulators, including *Pax7*, *Myf5*, *Myod1*, *Myog*, fusion-mediating
108 factors such as *Myomixer* (*Mymx*) and *Myomaker* (*Mymk*) was markedly reduced in $AR^{(i)sat-/Y}$ muscles
109 (Figure 1I), in agreement with the decreased MuSC number. Similarly, transcripts encoding contractile

110 cytoskeletal components such as actin, actinin, troponin and tropomyosin isoforms (e.g. *Actb*, *Actn1*,
111 *Actn4*, *Tnnc1*, *Tnnt2*, *Tpm3*), and embryonic myosin heavy chains isoforms (*Myh3*, embryonic and
112 *Myh8*, perinatal), as well as non-contractile components, including laminins (*Lmna*), *Myomesin 3*
113 (*Myom3*), and *Dystrophin* (*Dmd*), were significantly diminished (Figures 1G and 1I), providing a
114 molecular rationale for the morphological abnormalities observed at this timepoint. In agreement,
115 immunofluorescence analysis of DMD at 7 dpi revealed profound structural abnormalities in $AR^{(i)sat-/Y}$
116 mice compared to control littermates (Figure 1J). Moreover, co-staining for sarcomeric alpha actinin
117 (ACTN1) and DMD on transverse sections showed disrupted sarcomere alignment and uneven ACTN1
118 distribution in mutant fibers, while longitudinal sections confirmed major striation defaults (Figure 1K,
119 pink arrows). Notably, whereas healing control fibers had centrally positioned nuclei, $AR^{(i)sat-/Y}$ fibers
120 showed disorganized central nuclear localization (Figure 1K, white arrows), reflecting a disrupted
121 cytoskeletal organization. Consistent with our transcriptomic data, immunostaining for embryonic
122 myosin heavy chain (MYH3) at 5 and 7 dpi showed a ~50% reduction in the number of MYH3-positive
123 fibers in $AR^{(i)sat-/Y}$ mice compared to controls (Figures 1L and 1M), signifying delayed or incomplete
124 myogenic progression. To further investigate this impairment, we examined the expression profile of
125 myosin heavy chain isoforms (Figure 1N). In contrast to the downregulation of *Myh3* and *Myh8*,
126 transcripts of *Myh2*, *Myh4*, and *Myh7* (encoding MyHC IIa, IIb, and I, respectively) were upregulated
127 (Figure 1N), reflecting a shift toward increased expression of adult myosin heavy chain isoforms at the
128 expense of fetal ones, although *Myh1* (MyHC IIx) did not reach statistical significance (Figure 1N).
129 Interestingly, transcriptomic analysis of the 1,541 genes upregulated in 7 dpi-injured $AR^{(i)sat-/Y}$ TA
130 muscles revealed a predominant enrichment in metabolic pathways, particularly those governing
131 glycolysis, oxidative phosphorylation, mitochondrial function, and the metabolism of glycogen, fatty
132 acids, and amino acids (Figure 1H). Notably, expression of several key regulators of cellular
133 metabolism, including aconitase 2 (*Aco2*), citrate synthase (*Cs*), and multiple isoforms of isocitrate
134 dehydrogenase (e.g. *Idh2* and *Idh3a*), was markedly elevated in $AR^{(i)sat-/Y}$ muscles. This was paralleled
135 by increased expression of genes and components of the oxidative phosphorylation machinery,
136 including most of the members of mitochondrial complex I (e.g., *Ndufa1-13*), II (e.g., *Sdha-d*), III (e.g.,
137 *Uqcrc1-2*), IV (e.g., *Cox5a*, and *Cox10a*), and V (e.g., *Atp5a1* and *Atp5b*) (Figure 1O). Of note, the
138 expression of these genes was not affected in the absence of injury (Figures S1L and S1M).
139 To investigate whether the absence of MuSC-AR during regeneration promotes a metabolic shift
140 toward a more oxidative muscle fiber phenotype, we stained NADH dehydrogenase activity (NADH-
141 DH) 7 dpi. In regenerating TA muscles from control mice, we observed lightly stained fibers, indicative
142 of glycolytic metabolism. In contrast, $AR^{(i)sat-/Y}$ muscles displayed a higher presence of darkly stained
143 fibers (Figure 1P), reflecting increased NADH-DH activity. These findings were corroborated by

144 cytochrome c oxidase (COX) activity staining, indicative of a glycolytic-to-oxidative shift in fiber type
145 composition (Figure 1P). These findings prompted us to investigate whether such metabolic
146 alterations are intrinsically rooted in MuSC. Seahorse analysis performed on LHCN-M2 human
147 myoblasts, treated with 100 nM of the AR antagonist flutamide, unveiled an increased oxidative
148 phosphorylation activity when compared to vehicle-treated cells (Figures 1Q and S1N) indicating that
149 the metabolic abnormalities observed in regenerating myofibers may originate from intrinsic defects
150 in MuSC. In parallel, basal ECAR was measured for glycolysis analyses (Figures S1O and S1P).
151 Altogether, our data show that AR loss in young individuals leads to MuSC depletion and important
152 structural defects, associated with a fiber-type switch towards oxidative metabolism.
153
154 **Androgen signaling in MuSC coordinates gene programs essential for homeostasis and regeneration**
155 To elucidate the cell-specific AR-dependent molecular mechanisms governing MuSC homeostasis
156 during skeletal muscle regeneration, we performed a SMART-seq on FACS-isolated MuSC from 7 dpi-
157 injured TA of young (15-week-old) control and $AR^{(i)sat-/Y}$ male mice. Transcriptomic analysis revealed
158 differential expression of 821 genes in AR-deficient MuSC, including 327 down- and 494 upregulated
159 genes (Figures 2A and S2A). Consistent with the Seahorse assay findings and the histological evidence
160 of a metabolic shift toward oxidative metabolism at 7 dpi, analysis of the upregulated genes
161 highlighted a strong enrichment of pathways related to metabolic processes, particularly cellular
162 respiration and oxidative phosphorylation (Figure 2B). In particular, the expression of *Cox5b* and
163 *Cox6b1*, in addition to numerous genes implicated in mitochondrial homeostasis, was significantly
164 elevated in $AR^{(i)sat-/Y}$ MuSC (Figure 2C). Conversely, pathway analysis of the downregulated gene set
165 revealed a significant association with cell cycle regulation (e.g., DNA replication and cell division)
166 (Figures 2B and 2D).
167 To identify the direct transcriptional targets of AR, we isolated MuSC from TA muscles of control mice
168 by FACS at 7 dpi, and performed CUT&RUN assays using AR-specific antibodies, alongside profiling of
169 demethylated histone H3 (H3K4me2), a well-established marker of active promoters and enhancers.
170 Bioinformatic analysis identified 7,346 AR-binding peaks, predominantly located within intronic and
171 intergenic regions encompassing the canonical androgen response elements (AREs) (Figures 2E and
172 S2B), as well as 39,900 peaks associated with the H3K4me2 mark, evenly distributed between
173 promoter, intron and intergenic regions (Figure S2C). Integrative analysis of the two datasets revealed
174 that AR is directly recruited to 3,104 transcribed genes (Figure S2D). Gene ontology and pathway
175 enrichment analyses of AR-bound genes uncovered a strong association with key developmental and
176 regenerative pathways, including the HIPPO (e.g. *Tead1*, *Wwc1*, *Fat4*) and WNT signaling cascades
177 (e.g. *Wnt5a*, *Fzd4*), as well as signaling modules related to tissue remodeling and regeneration, such

178 as cell adhesion, focal adhesion, extracellular matrix (ECM)-receptor interactions, and actin
179 cytoskeleton regulation (Figure 2F). Notably, AR occupancy was also observed at genes essential for
180 stem cell homeostasis (e.g. *Foxo1*, *Bcl2*), muscle repair (e.g. *Mstn*, *Cxcl2*, *Cdh15*), and sarcomere
181 assembly or function (e.g. *Myh1*, *Mylk4*, *Myom2*). A transcription start site (TSS) gene-centric analysis
182 demonstrated that AR binds more than the two-thirds of both down- and upregulated genes in $AR^{(i)sat-}$
183 $^{/Y}$ mice within a 100-kb window (Figure 2G), showing that AR predominantly regulates gene expression
184 through distal elements. Representative AR binding loci within key genes involved in the
185 aforementioned pathways, including *Ar* itself, *Fzd4*, *Kdmc4*, *Myh1, Tead1*, and *Mylk4* are illustrated in
186 Figure 2H. Gene ontology analysis revealed that genes downregulated in association with AR peaks at
187 7 dpi were predominantly involved in cellular structural and organelle-related processes (Figure S2E),
188 whereas upregulated genes were enriched in metabolic pathways (Figure S2F), thereby providing a
189 molecular basis for the impaired phenotype observed at the histological level. Altogether, these
190 findings support a model in which AR orchestrates regenerative transcriptional programs in MuSC via
191 enhancer-driven mechanisms.
192

193 **Single-cell RNA sequencing reveals early molecular and cellular alterations in the AR-deficient MuSC**
194 **microenvironment**

195 To decipher the primary events underlying defective MuSC homeostasis caused by AR loss, and the
196 consequent impact on their microenvironment during impaired regeneration, we performed single-
197 cell RNA sequencing (scRNA-seq) in 5-dpi-injured TA muscles of young (15-week-old) control and
198 $AR^{(i)sat-/Y}$ mice (Figure S3A). Of note, $AR^{(i)sat-/Y}$ mice harbored the YFP transgene selectively in MuSC to
199 efficiently follow those cells. We identified 12 unsupervised clusters, annotated to the literature [29, 30],
200 based on the expression of specific marker genes (Figures 3A, S3A and S3B), with no evidence of cell
201 population loss or emergence in mutants (Figures 3A, 3B and Table S1 and S2). However, we observed
202 a slight reduction in the proportion of fibro-adipogenic progenitors (FAPs) and MuSC, as well as an
203 increase in that of both macrophages in $AR^{(i)sat-/Y}$ mice compared to controls (Figure 3B). Flow
204 cytometry analysis of injured TA muscles at 5 dpi, furtherly confirmed a ~30% increase in macrophages
205 number among $CD45^{+}$ immune cells (Figure 3C), and immunolabeling for F4/80 revealed an upward
206 trend in macrophage abundance (Figure S3C and S3D). In parallel, flow cytometry analysis indicated
207 an ~8% decrease in MuSC, while total immune cells and FAPs were not significantly altered (Figure
208 3D). Notably, *Ar* expression was not ubiquitous across all populations; rather, it was predominantly
209 detected in cell types exhibiting stem-like properties or mesenchymal profiles, including FAPs,
210 fibroblasts, and MuSC (Figure 3E). *Ar* expression was completely abolished in mutant MuSC, and not
211 in other cell types (Figure 3E), while *Yfp* was exclusively expressed in MuSC of $AR^{(i)sat-/Y}$ mice, consistent

212 with the genetic engineering of our model (Figure S3E). Moreover, AR deficiency in MuSC strongly
213 altered the transcriptional profile of their cellular microenvironment (Figure S3F).
214 To assess intercellular communication within injured muscle tissue at 5 dpi, we employed CellChat
215 analysis on scRNA-seq data. In control mice, this analysis revealed a highly interconnected signaling
216 network encompassing all cellular populations, indicative of active and coordinated crosstalk during
217 the regenerative process (Figures S3G and S3H). Interestingly, communication within the MuSC
218 population was diminished in AR$^{(i)sat-/Y}$ mice, as indicated by the decrease of the arrow thickness (Figure
219 3F), pointing to a disruption in intra-population signaling.
220 Given the critical interplay between MuSC, macrophages, and FAPs, we next examined the gene
221 networks affected by MuSC-AR loss within these two cell populations. Functional enrichment analysis
222 of the 1,707 differentially expressed genes upon AR loss in MuSC within macrophages uncovered a
223 transcriptional landscape indicative of macrophages homeostasis (Figure S3I). In particular, transcripts
224 encoding core components of the inflammasome pathway, including caspase 1 (*Casp1*) and its adaptor
225 *Pycard*, were elevated, alongside the chemokines C-C motif chemokine ligand 2 (*Ccl2*) and C-X-C motif
226 chemokine ligand 10 (*Cxcl10*), both of which are known to promote monocyte recruitment.
227 Furthermore, we observed enrichment in metabolic and proteasome pathways intimately linked with
228 immune regulation and tissue remodeling, including oxidative phosphorylation (e.g., *Cox6b1, Cox17*),
229 and ubiquitin-proteasome mediated degradation (e.g., *Uba3*) (Figure S3I). Moreover, macrophage
230 polarization analysis revealed robust expression of canonical pro-inflammatory markers including *Il1b*
231 and *Tnf*, in both control and mutant macrophages at 5 dpi (Figure 3G). In contrast, macrophages from
232 AR$^{(i)sat-/Y}$ mice expressed anti-inflammatory markers such as interleukin-10 (*Il10*) and peroxisome
233 proliferator-activated receptor gamma (*Pparg*) (Figure 3H), suggesting a precocious transition toward
234 an anti-inflammatory phenotype in mutant individuals. Further subclustering of the macrophage
235 population revealed that they did not constitute a homogeneous cluster, but instead, segregate into
236 five transcriptionally distinct subpopulations with specialized functional programs (Figures S3J-S3M).
237 Cluster 0 was characterized by high expression of pro-inflammatory markers such as *Ccr2*, *Il1b*, and
238 *Ccl5*, consistent with recently recruited, monocyte-derived macrophages (Figures S3J-S3L). Cluster 1
239 displayed a strong pro-inflammatory profile, marked by elevated expression of *Tnf*, *Ccl2*, *Ccl7*,
240 *Cxcl1/2/3*, interferon-stimulated genes (*Ifit1/2/3*), indicative of highly activated macrophages involved
241 in leukocyte recruitment and inflammatory amplification (Figures S3J-S3L). Cluster 2 corresponded to
242 phagocytic and lipid-associated macrophages, expressing canonical LAM markers including *Gpnmb*,
243 *Ctsd*, *Spp1*, *Fabp5*, *Lgals3*, and *Cd36*, suggesting a central role in debris clearance and lipid handling
244 during tissue remodeling (Figures S3J-S3L). Cluster 3 was enriched for genes involved in iron
245 metabolism and oxidative stress responses, such as *Slc40a1*, *Hmox1*, *Fth1*, and *Ftl1*, together with

246 *Marco*, *Spic*, and *Arg1*, consistent with specialized macrophages implicated in iron recycling and stress
247 adaptation (Figures S3J-S3L). Finally, Cluster 4 exhibited a tissue-resident, reparative phenotype
248 characterized by *Cd163*, *Lyve1*, *Mrc1*, *Retnla*, and *Folr2* expression, alongside extracellular matrix and
249 remodeling genes including *Col1a1*/2, *Sparc*, and *Gas6*, indicating anti-inflammatory, pro-reparative
250 functions (Figures S3J-S3L). Differential expression analysis across different populations further
251 revealed cluster-specific functional alterations, with altered antigen-presenting capacity, impaired
252 oxidative metabolism, and shifts toward migratory or scavenger states depending on the
253 subpopulation (Figure S3L). scRNA-seq analysis of macrophage populations revealed an increased
254 representation of an anti-inflammatory macrophage subcluster in $AR^{(i)sat-/Y}$ muscles (Figure S3M). To
255 further examine this observation at the injury site, we performed immunofluorescence labeling for
256 CD163, a marker associated with anti-inflammatory, pro-reparative macrophages. Quantification
257 revealed an increase in CD163 mean fluorescence intensity (MFI) in $AR^{(i)sat-/Y}$ TA muscles at 5 dpi
258 compared to controls (Figures S3N and S3O). These observations are consistent with our single-cell
259 RNA sequencing analysis, which identified a macrophage cluster enriched for *Cd163*, *Mrc1*, and *Folr2*
260 expression, indicative of tissue-resident, anti-inflammatory, and remodeling-associated macrophages
261 (Figures S3J and S3K).
262 To determine whether this aberrant immune environment persists over time, we extended our
263 analysis to 7 dpi. Flow cytometry revealed a three-fold increase in immune cells in $AR^{(i)sat-/Y}$ TA relative
264 to controls (Figure 3I), and immunofluorescent labeling of the macrophage-specific marker F4/80
265 exhibited an increasing trend of the signal (Figures 3J, white arrows, and 3K). Remarkably,
266 macrophages were frequently localized inside degenerating muscle fibers of $AR^{(i)sat-/Y}$ mice (Figure 3J,
267 red arrows, and 3K), a phenomenon typically restricted to early regenerative stages, thus indicating
268 delayed resolution of inflammation or prolonged clearance of necrotic tissue. CD163 levels were
269 comparable between $AR^{(i)sat-/Y}$ and control muscles, in contrast to the increased signal observed in
270 mutants at 5 dpi (Figures S3N and S3O). This temporal pattern may suggest that macrophages in $AR^{(i)sat-}$
271 $^{/Y}$ muscles transiently acquire reparative features at earlier stages of regeneration.
272 Together, these findings reveal that AR signaling in MuSC plays a pivotal role in modulating the
273 inflammatory response within the injured muscle by impacting the macrophage transcriptomic
274 repertoire.
275 To unravel the impact of AR loss in MuSC on FAPs transcriptional signature, we performed further
276 functional enrichment analysis of their 976 differentially expressed genes (Figure S3F). Pathway
277 analysis revealed upregulation of fibrosis-related transcripts, including *Tgfb*, alongside extracellular
278 matrix (ECM) remodeling enzymes, such as *Adamts* isoforms, *Mmp19*, *Serpine1*, and *Cthrc1*.
279 Moreover, we observed enhanced expression of key adipogenic regulators (*Zeb1*, *Cebpd*, *Socs1*, and

280 *Socs3*). Functional enrichment also highlighted disruptions in metabolic pathways, notably oxidative
281 phosphorylation (*Cox4i1*, *Cox5a*, *Cox6a1*) and aerobic respiration (*Aco2*, *Hadhb*, *Gls*, *Lipa*) (Figure S3P),
282 pointing toward a shift in FAPs identity, from pro-regenerative to fibrotic and adipogenic.
283 Interestingly, while FAPs numbers were comparable between genotypes at 5 dpi (Figure 3D), a two-
284 fold reduction was observed in $AR^{(i)sat-/Y}$ muscles by 7 dpi (Figure 3I). We therefore postulated that
285 decline might be attributed to differentiation of FAPs towards the fibrogenic or adipogenic lineages.
286 To this aim, we performed Sirius Red staining at 7 dpi on injured TA from control and mutant mice.
287 Mutant muscles displayed a marked increase in collagen deposition, with fibrotic area nearly doubled
288 compared to controls (Figures 3L and 3M, black arrows). These findings were corroborated by
289 Masson's Trichrome staining, which revealed a significant enrichment of collagen within the ECM at 7
290 dpi, with signs of early deposition already evident at 5 dpi in young $AR^{(i)sat-/Y}$ mice (Figure S3Q).
291 Polarized light microscopy revealed that the qualitative composition of the ECM, including collagenous
292 components such as collagens type I (Figures 3L, white arrows and 3N) and III (Figures 3L, cyan blue
293 arrows and 3N), and non-collagenous cones (e.g., fibronectin, laminins, elastin, tenascin-C, and
294 proteoglycans) remained comparable between genotypes, indicating a quantitative rather than
295 compositional remodeling. We further evaluated adipogenic conversion via perilipin-1 (PLIN1)
296 immunostaining. At 5 dpi, $AR^{(i)sat-/Y}$ muscles already showed early signs of adipocyte emergence, which
297 further increased by 7 dpi, whereas control muscles remained largely devoid of PLIN1-positive cells
298 (Figures 3O and 3P). Thus, our data demonstrate that AR loss in MuSC impacts FAPs differentiation
299 capacities promoting fibrosis and adipogenesis.
300 Altogether, these results indicate that AR signaling in MuSC plays a central role in coordinating the
301 regenerative niche by regulating the balance between pro- and anti-inflammatory immune responses
302 and controlling FAP fate (Figure 3Q).
303
304 **AR deficiency in MuSC at young age perturbs their stemness signatures, disrupts their commitment,**
305 **and impairs their differentiation potential**
306 Strikingly, only few genes were differentially expressed in MuSC, suggesting that different cell
307 populations might lay in this cluster (Figure S3F). To further explore the transcriptional changes
308 between control and $AR^{(i)sat-/Y}$ MuSC, we performed subclustering of MuSC following additional
309 stringent quality control, yielding a final dataset of 445 MuSC (Figures S4A and S4B). Unsupervised
310 clustering revealed six distinct MuSC subpopulations (Figure S4B), of which two clusters exhibited an
311 immune signature characterized by the expression of *C1qc*, *Lyz2*, and *Cd68* (Figures S4B and S4C).
312 Given recent findings describing these subsets as immuno-myoblasts in regenerating muscle [29, 31], we
313 hypothesized that these clusters represent MuSC targeted for immune-mediated clearance.

314 Consequently, we excluded these populations from our analysis and re-clustered the remaining four
315 subtypes based on their transcriptional profiles (Figures 4A, S4D, S4E and Table S3).
316 Our analysis delineated two distinct clusters of quiescent MuSC (clusters 0 and 1), both characterized
317 by the expression of *Pax7* and *Myf5*, while lacking *Myod1* and *Myog* expression (Figures 4A, 4B and
318 S4E). Moreover, we identified an activated MuSC subcluster (cluster 2) distinguished by the additional
319 expression of *Myod1* and the proliferation marker *Mki67* (Figures 4A, 4B and S4E). Importantly, a fully
320 committed myogenic cell population (cluster 3), characterized by *Myog* expression as well as that of
321 *Mymk* and *Mymx,* and originally absent in control individuals, emerged in mutant mice (Figures 4A,
322 4B, S4E, and S4F). In line with this observation, we found that *Ar* expression was confined to quiescent
323 clusters 0 and 1 in control mice, whereas ectopic *Myf5* and *Myod1* expression was noted in cluster 1
324 in $AR^{(i)sat-/Y}$ individuals (Figure 4B), indicating that loss of AR in MuSC promotes myogenic commitment.
325 Notably, several genes associated with symmetric division, including *Bmi1*, *Msi2*, and *Zfx*, were
326 upregulated in mutant mice within cluster 3 (Figure S4G), alongside a broader expression of the
327 fusogenic markers *Mymk* and *Mymx* across a larger subset of cells (Figure S4F), indicative of symmetric
328 differentiation.
329 To provide evidence of commitment defaults caused by loss of AR in MuSC, we assessed cell cycle
330 distribution within each cluster (Figures 4C and S4H). Our analysis revealed various perturbations upon
331 AR loss, including cells in G2/M in cluster 1 (Figure 4C). Moreover, in the fully committed cluster 3, the
332 proportion of cells in G1 dropped from ~80% in controls to ~60% in mutants, whereas those in S phase,
333 absent in control mice, increased by more than 15% in MuSC-AR deficient mice (Figure 4C), indicating
334 that they are more prone to mitotic activity.
335 To investigate the division modalities of MuSC, we performed a series of immunofluorescence
336 analyses. Double staining for PAX7 and KI67 in injured TA muscles from control and $AR^{(i)sat-/Y}$ mice at 5
337 and 7 dpi revealed a significant reduction in proliferating MuSC in mutant mice (Figures 4D-4F),
338 indicative of impaired symmetric stem cell divisions. Furthermore, double immunodetection of PAX7
339 and MYOG at 5 dpi showed a marked increase in $PAX7^+/MYOG^+$ cells, accompanied by a decrease in
340 $PAX7^+/MYOG^-$ cells upon AR loss in MuSC (Figures 4G and 4H). By 7 dpi, both $PAX7^+/MYOG^+$ and
341 $PAX7^-/MYOG^+$ cell populations exhibited a two-fold increase in $AR^{(i)sat-/Y}$ mice (Figures 4G and 4I),
342 supporting a shift from symmetric stem cell divisions toward an asymmetric division program.
343 To determine whether the absence of AR in MuSC alters their mode of division, we performed MYOG
344 and KI67 double immunostaining on injured TA muscles at 5 and 7 dpi. Notably, $MYOG^+/KI67^+$ double-
345 positive cells were detected within regenerating regions of mutant muscles (Figure 4J), consistent with
346 our scRNA-seq analysis showing an increased proportion of the committed cluster 3, characterized by
347 *Mki67* expression in mutants (Figure S4I). Quantification confirmed that $MYOG^+/KI67^+$ cells were more

348 abundant in AR$^{(i)sat-/Y}$ muscles at both 5 and 7 dpi (Figure 4K), indicating that MuSC prematurely engage
349 in the differentiation program. To further examine MuSC division behavior, single myofibers were
350 isolated from injured TA muscles at 7 dpi and analyzed *in vitro* to assess the orientation and
351 organization of satellite cell divisions. PAX7, KI67, and MYOG immunostaining revealed abnormalities
352 in AR$^{(i)sat-/Y}$ myofibers. Analysis of mitotic orientation on muscle fibers isolated from control and AR$^{(i)sat-}$
353 $^{/Y}$ mice showed perpendicular MuSC division in mutant fibers (Figure S4J), indicative of a shift toward
354 asymmetric differentiation, and suggesting disruption of the spatial control of MuSC division planes.
355 In addition, mutant fibers exhibited nuclear budding-like structures along the fiber surface, a feature
356 consistently absent in control fibers (Figure S4K). Overall, our data show that loss of AR in MuSC
357 promotes premature differentiation and alters division orientation toward asymmetric divisions.
358 We henceforth hypothesized that increased symmetric differentiation may deplete the stem cell pool,
359 compromising its ability to support effective repair during subsequent regenerative challenges. To test
360 this, we subjected control and AR$^{(i)sat-/Y}$ muscles to a secondary CTX-induced injury 28 days after the
361 primary injury, and assessed tissue morphology 7 days later (28+7 dpi). At this stage, control muscles
362 exhibited an accelerated regenerative response compared to muscles analyzed at 7 dpi following a
363 single injury (Figure 4L), consistent with previous reports [1, 32], reflecting a primed regenerative state.
364 This response was characterized by reduced immune cell infiltration (Figure 4L, cyan arrows), a
365 predominance of centrally nucleated myofibers (Figure 4L, black arrows), and minimal interstitial
366 matrix deposition (Figure 4L, green arrows). In contrast, AR$^{(i)sat-/Y}$ muscles displayed exacerbated
367 pathological features, including persistent immune infiltration (Figure 4L, cyan arrows),
368 multinucleated fibers with pronounced morphological abnormalities, and disorganized fibers with
369 fusion defects and nuclear mislocalization throughout the sarcoplasm (Figure 4L, pink arrows),
370 together with fat deposition (Figure 4L, red arrows). Immunolabeling for DMD further confirmed the
371 structural heterogeneity and irregularities in AR$^{(i)sat-/Y}$ muscles at 28+7 dpi (Figure 4M). These defects
372 were accompanied a threefold reduction in MuSC numbers in AR$^{(i)sat-/Y}$ mice compared to controls as
373 revealed by quantification PAX7-positive MuSC at 28+7 dpi (Figure 4N).
374 Overall, these results indicate that AR signaling in MuSC is essential for maintaining the stem cell pool
375 by promoting symmetric divisions and preventing premature differentiation (Figure 4O), thereby
376 ensuring effective regenerative capacity during both primary and subsequent injuries.
377
378 **AR controls MuSC fate through early chromatin remodeling**
379 To capture early AR-dependent chromatin events with the potential to drive the scRNA-seq-detected
380 transcriptomic alterations and downstream regenerative defects, we performed CUT&RUN profiling
381 of AR and the active chromatin mark H3K4me2 in young FACS-isolated MuSC at 5 dpi. Consistent with

382 our observations at 7 dpi, CUT&RUN analysis at 5 dpi identified 7,612 AR binding peaks, primarily
383 localized to intronic and intergenic regions (Figure S5A), associated with 7,040 genes. The majority of
384 these AR-bound loci coincided with H3K4me2 enrichment at promoter regions (Figures S5B and S5C).
385 Motif analysis using HOMER revealed that 50.6% of AR peaks contained canonical AR binding motifs
386 (Figure 5A), confirming the specificity of AR-DNA interactions. Functional enrichment analysis of AR
387 target genes demonstrated significant involvement in pathways critical for stem cell homeostasis and
388 tissue remodeling, notably the HIPPO and PI3K-Akt signaling pathways (Figure 5B). Similar to what we
389 described at 7 dpi, gene-centric analysis revealed that AR is mainly recruited within a 100-kb window
390 of more than 50% of differentially expressed genes (Figures 5C and 5D). Representative AR binding
391 loci at key genes involved in these regulatory pathways, including *Clock*, *Eifd2* and *Psma4*, are depicted
392 in Figure 5E. Together, these findings demonstrate that AR engages early with the MuSC chromatin
393 landscape, preferentially at distal regulatory elements enriched in active histone marks, to control the
394 transcriptional programs governing stem cell fate and tissue remodeling.
395
396 **AR dynamically repositions upon injury to govern time-dependent regenerative genomic programs**
397 The transcriptomic discrepancies observed between 5 and 7 dpi led us to question AR positioning on
398 the DNA during muscle repair. Deeptools analysis demonstrated minimal overlap and distinct peak
399 profiles for each state between AR-bound chromatin landscapes 0- (Basal), 5- and 7 dpi (Figures 5F-
400 5H). This temporal specificity was further confirmed by comparative analysis of the genes bound by
401 AR in those specific clusters (Figure 5F). The genes commonly controlled by AR during the regeneration
402 process were mainly implicated in cell-cell adhesion or in the connection with the synapse, essentially
403 *via* cadherins (e.g. *Cdh2*, *Cdh6*, *Cdh7*), and included *Ar* itself, and *Gli3* that is essential for MuSC injury
404 memory [33] (Figure 5G). More importantly, in the absence of injury, AR binding was enriched at genomic
405 loci associated with MuSC stemness, including *Pax3*, *Pax7*, and *Kdm1a* (*Lsd1*) (Figures 5G and 5H),
406 while AR-bound landscape profile markedly shifted at 5 dpi, targeting genes implicated in MuSC
407 activation, such as *Myf5* and *Tead1*, and asymmetric division like *Aurkb*, or muscle commitment
408 including *Myh4* and *Myh9* (Figures 5G and 5H). 7 dpi, AR was further reallocated to loci related to
409 myogenic differentiation such as *Myod1*, *Mef2a* and *Mef2d*, and asymmetric division like *Numb* and
410 *Pard3* (Figures 5G and 5H). Representative genes exhibiting AR binding loci in a temporal and stage-
411 specific manner during regeneration such as *Pax7*, *Myf5*, and *Myod1* are depicted in Figure 5H.
412 Collectively, these findings reveal that AR is dynamically repositioned in MuSC following injury,
413 engaging stage-specific genomic loci to orchestrate transcriptional programs that govern activation
414 and lineage commitment via MRFs (Figure 5I). This temporal chromatin remodeling ensures a

415 balanced stem-to-committed transition, safeguarding the MuSC pool for future regenerative demands
416 in young adults.
417
418 **Age-related regenerative decline in skeletal muscle is causally linked to diminished androgen**
419 **signaling**
420 Given the age-related decline in MuSC number and regenerative potential, we hypothesized that
421 diminished androgen signaling may underlie this process. We thus quantified serum testosterone
422 levels in mice at different ages and observed a progressive decrease from ~25 nmol/L in young mice
423 to a plateau of ~5 nmol/L in old ones (Figure 6A). This was accompanied by a corresponding decrease
424 in *Ar* expression at both the transcript and protein levels in non-injured (NI) TA muscle (Figures 6B-
425 6D), as well as a decrease in the number of MuSC expressing AR, compared to young mice (Figure
426 S6A). Notably, the transcript levels of the MuSC marker *Pax7* were diminished in NI TA of old control
427 mice (Figure 6E).
428 To determine the functional consequences of these baseline deficits, CTX injury was induced in 1-year-
429 old (hereafter old) control and mutant mice, derived from young mice treated with tamoxifen at 9
430 weeks and subsequently aged under natural conditions (Figure S6B). As expected, and consistent with
431 previous reports [10, 11], old male mice exhibited markedly impaired regenerative capacity compared to
432 young littermates (Figures S6C and S1K). To dissect the additional contribution of MuSC-specific AR
433 loss to this decline, we directly compared aged mutants to age-matched controls. Of note, while PAX7-
434 positive MuSC in control mice exhibited faint AR expression, it was entirely absent in $AR^{(i)sat-/Y}$ mutants
435 (Figures S6B and S6D). At 7 dpi, aged $AR^{(i)sat-/Y}$ muscles displayed increased interstitial space, sustained
436 immune infiltration, and misshaped regenerating fibers when compared to (Figure 6F). Ultrastructural
437 analysis confirmed these impairments, showing disrupted sarcomere organization, fragmented Z-
438 lines, and increased extracellular matrix deposition (Figure 6G). These structural impairments were
439 accompanied by a significant decrease in MuSC numbers (Figure 6H), and deformed regenerating
440 fibers (Figures 6I and S6E). In addition, recovery in aged muscles was accompanied by a pronounced
441 shift toward oxidative metabolism (Figure 6J), increased fibrosis (Figure 6K) and adipocyte emergence
442 (Figure 6L), highlighting the pivotal role of AR signaling in safeguarding the structural and functional
443 fidelity of regenerating muscle. Notably, the regenerative phenotype observed in aged control
444 muscles partially recapitulated features seen in young $AR^{(i)sat-/Y}$ mutants, whereas the combination of
445 aging and MuSC-specific AR loss further exacerbated these defects, highlighting the additive impact
446 of hormonal decline and receptor deficiency on regenerative capacity (Figure S6C).
447 To determine whether the regenerative impairment is causally linked to androgenic insufficiency, we
448 tested whether restoring androgen signaling could reverse aspects of the aged phenotype. We

449 thereby supplemented old mice with 5-α-dihydrotestosterone (DHT) implants. DHT supplementation
450 in old mice led to increased AR protein levels in gastrocnemius skeletal muscle 1 week after
451 implantation (Figures S6F). At 7 dpi, DHT-treated mice exhibited significantly improved muscle
452 regeneration, as evidenced by improved myofiber morphology, and an increased number of nuclei per
453 regenerating fiber (Figure 6M). Although the total number of MuSC was not significantly altered
454 (Figure 6N), we observed a slight increase in proliferating PAX7/KI67-double positive cells (Figure 6O),
455 which likely contributes to the increased number of centrally located nuclei and enhanced myogenic
456 fusion. Importantly, no significant differences were detected in differentiation capacity or immune
457 infiltration, as assessed by MYOG and F4/80 staining, respectively (Figures 6P and 6Q). In addition,
458 fibrosis analysis revealed a marked reduction in fibrotic area, with decreased collagen deposition
459 within the extracellular matrix (Figure 6R). Together, these findings provide direct evidence that age-
460 related androgen deficiency causally contributes to impaired aging skeletal muscle regeneration.
461
462 **Androgen signaling orchestrates distinct gene networks in young and old individuals leading to**
463 **similar phenotypes**
464 To understand how the age-related decline in androgen signaling affects MuSC regenerative
465 programs, we first compared the transcriptomic profiles of old control MuSC to those of young
466 counterparts at 7 dpi. This analysis identified 1,709 differentially expressed genes, including 798
467 downregulated and 911 upregulated transcripts (Figures 7A and S7A). Pathway enrichment analyses
468 of the downregulated gene set highlighted a significant suppression of pathways related to protein
469 synthesis and peptide/amide metabolism (Figure 7B), suggesting a reduced biosynthetic capacity in
470 aging MuSC. Notably, several genes essential for myogenic differentiation and structural regeneration
471 were significantly downregulated. These included *Myh4* and *Myod1* in addition to genes involved in
472 sarcomere organization and contractile function, such as nebulin (*Neb*), *Tpm3*, and troponin C type 2
473 (*Tnnc2*) (Figures 7A and 7C). This transcriptional repression is consistent with the defective
474 regenerative phenotype and histological and ultrastructural impairments observed in aged control
475 mice at 7 dpi. Conversely, pathway analyses on the 911 genes upregulated in MuSC from old control
476 mice compared to young control counterparts, revealed that these genes were predominantly
477 associated with metabolic and biosynthetic processes, notably the regulation of RNA, microRNA,
478 nitrogen metabolism, and nucleobase-containing compound metabolic pathways (Figures 7A and 7B),
479 but also oxidative metabolism processes (e.g. *Acadsb*, *Coq8b, Coq10b* and *Pdk4*) (Figures 7A and 7C),
480 collectively indicating a metabolic transition toward oxidative phosphorylation in old MuSC. These
481 molecular findings align with the histological evidence of enhanced oxidative metabolism observed at
482 7 dpi in old individuals.

483 Since aged control muscles exhibit histological and structural features reminiscent of young AR$^{(i)sat-/Y}$
484 ones, we next examined age-regulated genes to determine whether these shared changes involve AR-
485 dependent regulatory programs. To this end, we compared age-regulated genes with those
486 deregulated in young mutants and strickingly identified only 59 downregulated and 102 upregulated
487 genes common between young and aged MuSC (Figure 7D). Remarkably, a substantial fraction of
488 differentially expressed genes specific to aged MuSC exhibited AR binding within 100 kb of their TSSs
489 (Figures 7E and 7F), suggesting potential direct AR regulation. To assess the extent to which age-
490 associated transcriptional changes mimics AR loss in youth, we compared AR direct targets identified
491 in young mutant MuSC with age-regulated ones in old controls. This analysis revealed only limited
492 overlap with AR-bound genes (Figure 7G), indicating that the molecular mechanisms underlying AR
493 regulation in young MuSC differ from those driving age-associated transcriptional changes, even
494 though gene ontology analyses revealed similar functional enrichment (Figures S7D and S7F). This
495 limited convergence highlights that, while AR deficiency in MuSC at young age partially recapitulates
496 transcriptional features of aging, the molecular underpinnings differ, reflecting the distinct role of AR
497 during development as opposed to the combined decline of hormone and receptor signaling observed
498 in the elderly. Altogether, these findings support a model in which AR orchestrates regenerative
499 transcriptional programs in MuSC *via* enhancer-driven mechanisms, a regulatory framework that
500 persists with age but becomes functionally altered.
501 To extend our findings to a human model, we determined AR expression in LHCN-M2 and C79
502 myoblasts, isolated from young and aged male individuals, respectively. Notably, AR expression was
503 reduced by approximately 50% in C79 compared to LHCN-M2 myoblasts at both the transcript (Figure
504 7H) and protein levels (Figures 7I and 7J), in addition to the PAX7 levels (Figure 7K). Moreover, LHCN-
505 M2 cells displayed a higher propensity for proliferation (Figures 7L and S7I) and differentiation
506 compared to C79 cells (Figure 7M), mirroring the differences observed between young and aged mice.
507 In agreement, AR knockdown in both cell lines strongly impaired differentiation, as indicated by the
508 conservation of a fibroblast-like morphology, and lack of the characteristic spindle-shaped structure
509 observed in control cells, 5 days post-differentiation (dpd) (Figures 7M, S7J and S7K). Conversely, while
510 AR overexpression did not have flagrant effects on LHCN-M2 cells differentiation, a premature more
511 efficient myogenesis was observed in C79 cells, in the presence of elevated AR levels (Figures 7M, S7L-
512 S7N). Collectively, these findings demonstrate that intact AR signaling, requiring both sufficient ligand
513 and receptor, is essential for efficient myoblast differentiation, and by extension, effective skeletal
514 muscle regeneration.

515 **DISCUSSION**

516 Maintenance of the MuSC reservoir requires mechanisms that preserve quiescence, while ensuring
517 that repair proceeds with structural and functional fidelity. In young male skeletal muscle, AR
518 expression concentrates in the most quiescent, self-renewing MuSC states, and is largely extinguished
519 as cells commit. Conditional loss of AR in MuSC disrupts dormancy, accelerates cell-cycle entry, and
520 drives symmetric differentiation on the expense of stem cells renewal, leading to attrition of the
521 regenerative pool. Notably, bulk RNA-seq at 7 dpi reveals significant impairments in *Pax7*, *Myf5*,
522 *Myod1*, *Myog*, and *Mymx* expression in $AR^{(i)sat^{-}/Y}$ cells, whereas scRNA-seq at 5 dpi does not detect
523 these changes. This discrepancy reflects differences in both regeneration stage and analytical
524 resolution as bulk RNA-seq captures population-wide transcriptional shifts later in repair, whereas
525 scRNA-seq interrogates cell-state-specific signatures at an earlier time point, without implying a
526 biological inconsistency. On this basis, we here identify AR as lineage-intrinsic indicator of MuSC
527 stemness in males, functionally distinct from its canonical anabolic role in myofibers [16, 25, 26, 34].

528 This AR-stemness relationship fits within a broader endocrine framework across the male life course.
529 At young age, androgens promote the establishment of a long-lived quiescent MuSC pool from
530 juvenile precursors through a Notch-dependent pathway [18]. With aging, declining systemic androgens
531 correlate with reduced MuSC number and impaired repair [35], and androgen supplementation restores
532 regenerative capacity in low-androgen settings [36, 37]. Consistent with this trajectory, our MuSC-specific
533 AR knockout phenotypically recapitulates features of aging-associated stem cell exhaustion, including
534 reduced responsiveness to repeated injuries, suggesting that androgen decline and diminished AR
535 activity converge on shared mechanisms that erode the MuSC reservoir. It is worth noting, however,
536 that transcriptomic differences observed between AR-deficient young MuSC and those from aged
537 controls may also reflect distinct underlying causes, namely, the selective inactivation of AR in
538 otherwise intact young MuSC versus the broader loss of stem cells with age, along with age-related
539 alterations in the muscle microenvironment [38]. These observations indicate that androgen decline and
540 AR loss exert distinct yet complementary effects, the former reduces stem cell abundance and
541 responsiveness, while the latter disrupts intrinsic programs of quiescence and fate. In aged AR-
542 deficient mutants, these deficits appear to sum, producing an exacerbated phenotype that
543 underscores the dual contribution of hormone and receptor to MuSC maintenance.

544 We also observe that AR expression in young individuals persists for weeks after injury in MuSC
545 derived from self-renewal, reflecting early symmetric divisions driven by AR that maintain the
546 quiescent stem pool for future regenerative demands. In contrast, differentiating MuSC gradually lose
547 AR, showing that AR not only supports stem cell expansion, but also controls asymmetric divisions to
548 produce committed cells for repair. Without AR, MuSC divisions favor committed daughters over self-

549 renewal, depleting the reserve and impairing regeneration after repeated injury. This AR-dependent
550 balance between renewal and differentiation in male MuSC has not been shown *in vivo* before. Earlier
551 studies using female-derived C2C12 myoblasts showed DHT enhances proliferation, but these cells
552 lack true quiescence and do not represent adult male muscle stem cells [20, 42, 43]. In contrast, our findings
553 reveal that physiological androgen levels *via* AR in male MuSC dynamically regulates their fate during
554 regeneration.
555 MuSC-AR influences more than lineage fate in skeletal muscle. It promotes proliferation and
556 differentiation in myogenic cells [44, 45], and its loss in our mouse model leads to fusion defects, fiber
557 orientation defaults, and impaired ultrastructure, reflecting not only reduced progenitor output, but
558 also a disrupted regenerative program in these progenitors. This contradicts earlier claims that MuSC-
559 AR is dispensable for regeneration (Sakai et al., 2020), likely because their model did not disrupt AR in
560 the early, true stem MuSC population. Our data clearly establish MuSC-intrinsic AR as a crucial
561 regulator of androgen-driven muscle repair in males. This signaling axis also shapes metabolic identity.
562 While myofiber-AR supports glycolytic metabolism, its absence in MuSC at young age shifts
563 regenerated fibers toward oxidative pathways, which was recapitulated in aged individuals. Seahorse
564 assays and histology confirm this shift, consistent with findings in AR-deficient myofibers [25, 46], AR-
565 related disorders [47], and aging muscle [48, 49]. Notably, myofiber-AR loss is linked to increased β-oxidation
566 gene expression and reduced Complex IV components [25, 50], though this latter feature was absent in
567 our model, possibly due to reactive oxygen species accumulation impairing electron transport and
568 causing mitochondrial stress [51].
569 At the tissue level, MuSC-AR deletion in young individuals reveals increased inflammation, fibrosis,
570 and adipocyte accumulation at the site of injury. Similar disturbances occur in androgen-deprived
571 states, where impaired inflammatory resolution and accelerated fibro-adipogenic drift are observed
572 [52, 53]. These findings show that MuSC are not passive recipients, but active transmitters of androgen-
573 sensitive signals shaping their microenvironment. This supports a bidirectional model in which AR in
574 MuSC governs intrinsic fate decisions while orchestrating stromal and immune crosstalk during muscle
575 repair. While our data indicate that MuSC-AR influences macrophages and FAPs, these effects are
576 likely indirect. CellChat analysis did not reveal significant differences in secreted signaling molecules,
577 and *in vitro* co-culture experiments were precluded by the poor adherence of FACS-isolated $AR^{(i)sat^{-}/Y}$
578 MuSC. Therefore, MuSC-AR appears to shape the regenerative niche predominantly through indirect
579 intercellular mechanisms. Importantly, in AR-deficient muscles, macrophages prematurely express
580 anti-inflammatory markers, yet the total inflammatory burden persists longer, reflecting an
581 uncoupling between phenotypic transition and effective clearance. This aberrant trajectory likely
582 contributes to impaired regeneration and highlights the nuanced role of MuSC-AR in coordinating the

583 immune niche. Our CellChat analysis further suggests that AR-deficient MuSC perturb intercellular
584 communication with macrophages and FAPs, although the precise signaling mediators remain to be
585 defined. Identifying these factors represents a compelling avenue for future work, as it would
586 illuminate the mechanisms by which MuSC orchestrate niche remodeling and coordinate
587 regeneration.
588 To coordinate these diverse, stage-specific functions during muscle regeneration, we propose a
589 dynamic chromatin occupancy model in which AR sequentially engages distinct transcriptional
590 programs as MuSC progress from quiescence through activation to commitment. Such nuclear
591 receptor mobility and partner switching are well documented in other systems [54-57]. Emerging
592 evidence in skeletal muscle shows AR collaborates with SMAD signaling to enhance BMP-driven
593 transcriptional programs that regulate muscle mass and quality [58]. In aging and pathological
594 expansions of the AR-polyglutamine tract, altered chromatin binding and disrupted co-factor
595 interactions have been observed [59, 60], suggesting that reduced AR availability with age may limit its
596 genomic sampling and assembly of stage-specific complexes necessary to maintain stemness, and
597 sequentially enable differentiation.
598 In sum, MuSC-AR preserves quiescence, sustains the stem cell pool, shapes glycolytic identity, and
599 orchestrates niche remodeling. Its decline leads to reserve loss, metabolic drift, and regenerative
600 failure (Figure S7O), highlighting MuSC-AR as a therapeutic target in aging and disease.
601

602 **METHODS**

603 **Mouse Studies**

604 ***Housing***

605 Mice were maintained on a C57BL/6 background and housed in a temperature- and humidity-
606 controlled facility under a 12-hour light/dark cycle, with *ad libitum* access to standard rodent chow
607 (2800 kcal/kg, Usine d'Alimentation Rationelle, Villemoisson-sur-Orge, France) and water. Breeding
608 and maintenance followed institutional guidelines, and all experiments were conducted in an
609 accredited facility in compliance with French and EU regulations on laboratory animal use (Directive
610 2010/63/EU). Procedures were approved by the local ethical committee (Com'Eth, Strasbourg, France)
611 and by the French Ministry of Research (MESR). Mice were euthanized *via* cervical dislocation, and
612 muscles were harvested for histological and molecular analysis.

613

614 ***Generation of AR$^{(i)sat-/Y}$ mutant mice***

615 For satellite cell-specific androgen receptor (AR) ablation, AR$^{L2/L2}$ female mice, carrying LoxP sites
616 flanking chromosome X exon 1 encoding the AR N-terminal domain [61], were intercrossed with *Pax7*-
617 CreER^{T2} male mice [62] to generate *Pax7*-CreER^{T2}/AR$^{L2/Y}$ mice, which express CreER^{T2} recombinase
618 selectively in satellite cells. To induce recombination, 9-week-old AR$^{L2/Y}$ control males and their *Pax7*-
619 CreER^{T2}/AR$^{L2/Y}$ pre-mutant littermates received intraperitoneal tamoxifen injections (1
620 mg/mouse/day) for five consecutive days, generating control and AR$^{(i)sat-/Y}$ mutant mice. Alternatively,
621 mice were intercrossed with a *Rosa26*-YFP reporter line [63] to generate *Pax7*-CreER^{T2}/AR$^{L2/Y}$/*Rosa26*-
622 YFP$^{Tg/0}$ mice with one YFP allele, allowing selective labeling of satellite cells and lineage tracing of their
623 progeny. *Pax7*-CreER^{T2}/Rosa26-YFP$^{Tg/0}$ mice lacking the floxed AR allele were used as additional
624 controls. Mice were analyzed at 3 months of age (young adults) or at 1 year of age (aged cohort).
625 Primer sequences required for genotyping PCR are listed in Table S4.

626

627 ***Mouse Treatments***

628 For cardiotoxin-induced muscle injury model, 3 months young adults or at 1-year aged mice were
629 anesthetized with 2.5% isoflurane using a SomnoSuite device. To induce muscle damage, 20 µl of
630 25 µM cardiotoxin (CTX) (Latoxan, Valence, France, L8102), dissolved in phosphate-buffered saline
631 (PBS) were injected into the tibialis anterior (TA) muscle.

632 For androgen supplementation, 5-alpha-dehydrotestosterone (DHT) implants were inserted
633 subcutaneously in the intrascapular region of 21-month-old wild-type male mice, as described [64].
634 Muscle injury was induced by CTX injection three weeks post-implantation to avoid off-target effects
635 caused by DHT-burst.

636 **Testosterone serum levels measurement**

637 Blood was collected from mice in 50 mM EDTA tubes (Sigma-Aldrich), and plasma was isolated by
638 centrifugation at 3,000 g for 15 minutes at 4°C. The supernatant was collected, and serum
639 testosterone levels were quantified using the Testosterone Rat/Mouse ELISA Kit (LDN, AR E-8000R),
640 following the manufacturer's instructions.

641

642 **Contractile Measurements**

643 *In situ* isometric TA muscle force in response to nerve stimulation was measured as described [26]. In
644 brief, specific maximal tetanic force (mN/mm^2) was determined by dividing the measured force by the
645 estimated CSA of the muscle. Assuming a cylindrical muscle shape with a density of 1.06 mg/mm^3, the
646 CSA was calculated as the volume of the muscle divided by its (muscle) length. The optimal muscle
647 length (L0) was defined as the length at which maximal tetanic force was observed. All data collected
648 from the muscle lever system were recorded and analyzed using a microcomputer with the
649 PowerLab/4SP system (AD Instruments).

650

651 **Histological analyses**

652 ***Muscle histology***

653 Muscles were either snap-frozen in liquid nitrogen-cooled isopentane for cryosections, or fixed in 4%
654 PFA overnight at 4 °C then washed in PBS and 70% ethanol and embedded in paraffin. 10 µm thick
655 cryosections were prepared at −20 °C using a 2800 Frigocut cryostat (Leica, St Jouarre, France) and
656 kept at −20 °C until further analysis. 5 µm thick paraffin sections were cut at room temperature (RT)
657 using a microtome (Leica RM, 2145, 0737/09.1998) and stored at 4 °C until further analysis.
658 Hematoxylin and eosin, and Masson's Trichrome staining were performed on paraffin sections as
659 described, while NADH and COX staining were assessed on cryo-sections as described [25, 63, 65].

660

661 ***Quantification of Collagen Deposition***

662 Collagen content assessed by Sirius Red staining (Picro-Sirius Red Stain, Pint, StatLab, STPSRPT) was
663 imaged under a bright-field microscope, or under polarized light using the Axioscan 7 (Carl Zeiss) slide
664 scanner. Birefringent collagen fibers were visualized based on their differential light refraction
665 properties, allowing for the selective detection of collagen deposition. Quantification was performed
666 by analyzing the polarized signal intensity and distribution across the tissue using standardized image
667 analysis parameters established by the in-house anatomic pathology platform.

668

669

670 ***Immunofluorescence staining***

671 Paraffin and cryo-sections were processed using distinct protocols tailored to antibody requirements.
672 Paraffin sections underwent deparaffinization, and antigen retrieval was done under controlled
673 temperature and pressure conditions for 20 min in either tris-hydroxymethyl-aminomethane (Tris
674 buffer) (pH=9.0) or in Signal Stain ® Citrate Unmasking Solution (Cell Signalling 14746S). In contrast,
675 frozen sections were fixed for 10 min in 4% PFA at RT, and permeabilized with PBST for 15 min at RT.
676 Afterwards, paraffin or frozen sections were incubated overnight at 4 °C with the primary antibodies
677 diluted in PBST directed against AR (Rabbit, Abcam, ab108341, 1:500), PAX7 (Rabbit; Thermo Fisher,
678 PA1-117, 1:400, or Mouse; DSHB, AB_528428, 1:50), MYOG (Abcam, ab1835, 1:400), ACTN1 (Mouse,
679 Abcam, ab9465, 1:400), DMD (Mouse, IGBMC , 1Dystro1D2, 1:1000 or Rabbit sigma, D8168, 1:400),
680 KI67 (Rat, R&D systems, 14-5698-82, 1:500), LAMA2 (Rat, Sigma Aldrich, L0663-.1ML, 1:500), eMyHC
681 (Mouse, DSHB, F1.652, 1:20), F4/80 (Rabbit, Cell Signaling, 70076, 1:400) and PLIN1 (Rabbit, Abcam,
682 Ab3526. 1:200). Mouse (Santa Cruz Biotechnology, E3117, 1:500), rat (Vector Laboratories, BA-4000,
683 1:500) or rabbit (PeproTech, 500-P000-500UG, 1:500). IgGs were used as controls. Sections were
684 rinsed with wash buffer, and incubated with appropriate Alexa-Fluor-conjugated secondary antibodies
685 with different fluorescent wavelengths (488, 555 or 647 nm, 1:500, Invitrogen: a32732, a32723,
686 a21206, a21424, a48265, a32733, a32728) in permeabilization buffer for 45 min at RT. After wash,
687 slides were mounted with Fluoromount™ Aqueous Mounting medium containing DAPI (Invitrogen,
688 00-4959-52).

689

690 ***Fiber cross-sectional area measurements***

691 Muscle cross-sections were stained with DMD (Abcam, ab15277, 1:500) mark the sarcolemma
692 surrounding each fiber. CSAs were quantified using QuPath (open-source image analysis software)
693 integrated with a customized Groovy macro (available via GitLab). In brief, individual fibers were
694 identified based on the intensity and continuity of the stained sarcolemma surrounding each fiber by
695 segmentation. Areas were measured after background subtraction and automated thresholding.

696

697 ***Quantification of F4/80 and CD163 mean fluorescence intensity (MFI)***

698 Fluorescence images of injured TA muscles immunostained for F4/80 and CD163 were analyzed using
699 QuPath software (QuPath-0.5.0). Regions of interest (ROIs) corresponding to the injured areas were
700 annotated manually, and a pixel classifier was trained on these annotations to categorize pixels as
701 background/negative, positive signal, or other non-positive signals. Fluorescence intensity thresholds
702 were set manually for each marker to ensure accurate detection of positive staining. Mean

703 fluorescence intensity within the annotated ROIs was then measured and exported for further
704 analysis.
705
706 ***Muscle ultrastructural analysis***
707 1 mm² TA muscle samples were fixed overnight at 4°C by immersion in a mix of 2.5% glutaraldehyde
708 and 2.5% paraformaldehyde diluted in 0.1 M cacodylate buffer (pH 7.4), washed in the same buffer
709 for 30 min, and stored at 4°C. Post-fixation was performed with 1% osmium tetroxide in 0.1 M
710 cacodylate buffer for 1 h at 4°C, followed by dehydration through a graded ethanol series (50%, 70%,
711 90%, and 100%) and propylene oxide (30 min each). Samples were oriented longitudinally or
712 transversally and embedded in Epon 812. 70 nm ultrathin sections were obtained and contrasted with
713 uranyl acetate and lead citrate. Imaging was performed at 70 kV using a Morgagni 268D electron
714 microscope, with digital acquisition via a Mega View III camera (Soft Imaging System).
715
716 **Cell culture analyses**
717 ***Cell culture and treatments***
718 LHCN-M2 and C79 cells were cultured in Dulbecco's Modified Eagle Medium (DMEM 4,5 g/L of glucose,
719 Invitrogen 4165-062)/Medium 199 (Invitrogen 22340-020) (4:1), supplemented with 20% fetal calf
720 serum (FCS), 25 µg/mL fetuin, 5 µg/mL human insulin, 40 µg/mL gentamycin and 0.5 ng/mL basic
721 fibroblast growth factor (bFGF) along with 5 ng/mL human epidermal growth factor (hEGF) and 0.2
722 µg/mL dexamethasone [66]. Cells were maintained at 37°C in a humidified atmosphere with 5% CO_2.
723 Cells were split at 70-80% confluence, and the medium was replaced every 48 hours.
724 To induce differentiation, LHCN-M2 and C79 cells were seeded at 90% confluence and switched at
725 confluence to differentiation medium (DMEM supplemented with 2% horse serum and 40 µg/mL
726 gentamycin) for up to 5 days, with medium changes every 48 hours.
727 For transfection, human AR siRNA (5'-GGGCACTTCGACCATTTCTGA-3'), or scramble siRNA (5'-
728 AAGCTTCATAAGGCGCATAGC-3'), were introduced using Typical RNAiMAX Transfection kit
729 (ThermoFischer, 13778075), following the manufacturer's protocol. Cells were seeded in six-well plate
730 and transfected with 50 nM siRNA diluted in Opti-MEM (Gibco, USA) at 50-60% confluence for 24h,
731 after which the medium was replaced with fresh differentiation or growth medium. Cells were
732 subsequently treated with 100 nM of DHT (Sigma, A8380-1G) diluted in ethanol 24h after
733 transfections.
734 For AR overexpression, MuSC were transfected with the pEGFP-AR^{WT} plasmid using Lipofectamine
735 2000 DNA Transfection kit (ThermoFisher, 11668027), according to the manufacturer's instructions.
736 Cells were seeded in six-well plate and transfected with 14 µg pEGFP-AR^{WT} plasmid diluted in Opti-

737 MEM (Gibco, USA) at 50-60% confluence for 24h, after which the medium was replaced with fresh
738 differentiation or growth medium. Cells were subsequently treated with 100 nM of DHT (Sigma,
739 A8380-1G) diluted in ethanol 24h after transfections.
740
741 ***Cell Proliferation Analysis***
742 Cell proliferation was assessed using the CellTrace™ CFSE (Carboxyfluorescein Succinimidyl Ester)
743 Assay (Thermo Fisher Scientific, USA, C34557) as described [67]. Briefly, LHCN-M2 and C79 cells were
744 incubated with 5 µM CFSE at 37°C for 20 min in a humidified atmosphere with 5% CO_2. The labeling
745 reaction was quenched by adding an equal volume of complete growth medium, followed by two
746 washes with PBS to remove excess dye. Labeled cells were kept in appropriate culture conditions and
747 collected at 24-, 48-, and 72-hours post-labeling for flow cytometry analysis. CFSE fluorescence
748 intensity was measured using a flow cytometer (BD LSRFortessa™, BD Biosciences, USA) with
749 excitation at 488 nm and emission detection at 530 nm. Data were analyzed using FlowJo software
750 (BD Biosciences, USA), and cell proliferation was determined by monitoring the progressive dilution
751 of CFSE fluorescence across multiple cell generations. To identify non- and slow-proliferating cells, we
752 defined the 30% of cells exhibiting the highest CellTrace Violet signal in control as the reference
753 population, and calculated the proportion of cells with equal or greater signal intensity.
754
755 ***Immunocytochemistry***
756 Immunocytofluorescence assay was performed by incubating fixed LHCN-M2 and C79 cells with AR
757 (Rabbit, Abcam, ab108341, 1:500) and PAX7 (Mouse; DSHB, AB_528428, 1:50) antibodies.
758 Observations were made under a Leica confocal microscope.
759
760 ***Seahorse analysis of LHCN-M2 myoblasts***
761 Mitochondrial respiration was assessed using the Seahorse XF Cell Mito Stress Test Kit (Agilent
762 Technologies, Part Number: 103015-100) according to the manufacturer's protocol. Briefly, ~1800
763 LHCN-M2 myoblasts were seeded in Seahorse XF cell culture microplates (Agilent), and treated with
764 either vehicle or 100 nM flutamide (Abcam, ab141234) for 1 hour. The assay was performed on a
765 Seahorse XFe96 Analyzer (Agilent), following the sequential injection of oligomycin (1 µM), FCCP (2.5
766 µM), and rotenone/antimycin A (1 µM). Basal respiration, ATP-linked respiration, maximal respiration,
767 and spare respiratory capacity were calculated using Wave software (Agilent).
768
769
770

771 **Flow cytometry analysis**

772 ***Muscle cell populations composition***

773 Muscle stromal vascular fraction was isolated as described [68]. Briefly, hind limb muscles were
774 dissected, minced into small fragments, and enzymatically digested with 1.25 U/mL Dispase II
775 (Stemcell Technologies, Cat: 07913) and 500 µg/mL Collagenase Type I (Thermo Fisher Scientific,
776 17018029). The resulting cell suspension was sequentially filtered through 100 µm, 70 µm, and 40 µm
777 cell strainers (Corning Life Sciences) to remove debris. Cells isolated from digested muscle tissue were
778 stained with CD45 Alexa eFluor700 (eBioscience, 56-0451-82, 1:100), CD31 PE (eBioscience, 12-0311-
779 82, 1:100), SCA-1 PE-Cy7 (eBioscience, 25-5981-82, 1:100), and Integrin-α7 (ITGA7) FITC (MBL, K0046-
780 4, 1:50). Cells were analyzed based on forward scatter (FSC) and side scatter (SSC) parameters to
781 exclude debris and doublets. CD45- and CD31-positive cells were quantified to assess immune and
782 endothelial cell populations, respectively. After removing CD45/CD31-expressing cells, SCA-1-positive
783 cells were gated to identify fibro-adipogenic progenitor cells (FAPs). Finally, SCA-1-negative, ITGA7-
784 positive cells were classified as satellite cells. Fluorescence intensity was measured using a flow
785 cytometer (BD FACSymphony A1™, BD Biosciences, USA). Analysis were conducted using FlowJO
786 software as described [68].

787

788 ***Muscle immune cell populations composition***

789 Cells isolated from digested muscle tissue were stained with CD45 Alexa eFluor700 (eBioscience, 56-
790 0451-82, 1:100), CD11b PerCP-Cy5.5 (BioLegend, 101228, 1:100), Ly-6G-GR-1 FITC 488 (BioLegend,
791 108417, 1:100), Ly-6C PE-CF594 (BD Horizon™, AB_2737749, 1:100), and F4/80 APC eFluor 780
792 (eBioscience™, 47-4801-82, 1:100). Cells were analyzed based on forward scatter (FSC) and side
793 scatter (SSC) parameters to exclude debris and doublets.

794 Data analysis was performed by sequential gating on single, live $CD45^+$ leukocytes, followed by
795 identification of myeloid cells as $CD11b^+$, neutrophils as $CD11b^+Ly6G^+$, monocytes as
796 $CD11b^+Ly6G^-Ly6C^+$, and macrophages as $CD11b^+Ly6G^-$ $Ly6C^-F4/80^+$. Fluorescence intensity was
797 measured using a flow cytometer (BD FACSymphony A1™, BD Biosciences, USA). Analyses were
798 conducted using FlowJO software.

799

800 **Fluorescence-Activated Cell Sorting (FACS) of Satellite Cells**

801 After stromal vascular fraction isolation, mononucleated cells were pelleted by centrifugation at 400g
802 for 5 min, resuspended in FACS buffer (DMEM without phenol red, 4.5 g/L glucose, 2% BSA, 2 mM
803 EDTA), and labeled with fluorescence-conjugated antibodies. Cells were stained with CD45 PE
804 (eBioscience, 12-0451-83, 1:100), CD11b PE-Cy7 (eBioscience, 25-0112-82, 1:100), CD31 PE

805 (eBioscience, 12-0311-82, 1:100), TER119 PE (BD Pharmingen™, 553673, 1:100), ITGA7 FITC (MBL,
806 K0046-4, 1:50), CXCR4 APC (eBioscience, 17-9991-82, 1:100), and CD34 eFluor405 (eBioscience, 48-
807 0341-82, 1:33). Cells were gated based on FSC and SSC parameters to exclude cellular debris and
808 doublets. Leukocytes and endothelial cells were removed by gating out CD45-, CD11b-, CD31-, and
809 TER119-positive populations. The remaining fraction was further gated for CD34 and ITGA7
810 expression, and double-positive cells were selected based on CXCR4 expression. Fluorescence
811 intensity and sorting were conducted using a FACS sorter (BD FACSAria™, BD Biosciences, USA). Sorted
812 satellite cells were subsequently processed for RNA extraction or CUT&RUN analyses.
813
814 **CUT&RUN Assay and Bioinformatics Analysis**
815 CUT&RUN was performed as described [68, 69]. Briefly, FACS-isolated satellite cells were centrifuged at
816 500 g for 10 min at 4°C, and the resulting cell pellet was incubated with nuclear extraction buffer
817 (20mM HEPES-KOH pH = 7.9, 10 mM KCl, 0.5 mM Spermidine, 0.1% Triton X-100, 20% Glycerol and
818 protease inhibitor cocktail) for 20 min on ice. Isolated nuclei were then washed and incubated with
819 Concanavalin A-coated beads (BioMag Plus Concanavalin A, Cat: 86057-3) for 10 min at 4°C. Following
820 additional washes, the nuclei-bead complexes were incubated overnight at 4°C with gentle agitation
821 in the presence of primary antibodies targeting AR (Abcam, ab108341, 1:100) and H3K4me2 (Active
822 Motif, 39141, 1:100), and a Rabbit IgG (PeproTech, 500-P000-500UG, 1:100). Nuclei-bead complexes
823 were precipitated and incubated with protein A-micrococcal nuclease (pA-MN, IGBMC) for 1 h at 4°C
824 under constant agitation. Enzymatic cleavage was initiated by adding 3 µL of 100 mM $CaCl_2$, followed
825 by 30 min of incubation on ice. The reaction was terminated at 37°C for 20 min using stop buffer (200
826 mM NaCl, 20 mM EDTA, 4 mM EGTA, 50 µg/mL RNase A, 40 µg/mL glycogen, 25 pg/mL yeast spike-in
827 DNA). DNA was extracted from immunoprecipitated samples for sequencing.
828 Libraries were generated from immunoprecipitated DNA as described [68], and sequenced on an
829 Illumina HiSeq 2000 platform. Reads overlapping ENCODE blacklist regions (V2) were removed, and
830 deduplicated unique reads were conserved for further analysis. Reads were mapped to the mm10
831 reference genome using Bowtie2 (v2.3.4.3) [70]. To generate genome-wide intensity profiles, uniquely
832 mapped reads were processed as follows: Bigwig files were generated using bamCoverage (deeptools
833 3.3.0) [71], with normalization by RPKM (--normalizeUsing RPKM --binSize 20). Raw bedgraph files were
834 produced with genomeCoverageBed (bedtools v2.26.0) [72]. Peak calling was performed using SEACR [73]
835 and MACS2 [74] with IgG-immunoprecipitated samples as controls (-keepall), and peaks with an FDR at
836 least less than 0.05 were retained for further analysis. The IGV genome browser
837 (http://software.broadinstitute.org/software/igv/) was used for genome-wide intensity visualization.
838 Peaks were annotated, and motif analysis was conducted using HOMER. Genomic feature distribution

839 (promoters/TSS, 5' UTRs, exons, introns, 3' UTRs, transcription termination sites, and intergenic
840 regions) was determined based on RefSeq and HOMER annotations. For bioinformatics and clustering
841 analysis, Venn diagrams were generated using Venny (2.1.0)
842 (https://bioinfogp.cnb.csic.es/tools/venny/).
843 Clustering analyses were performed using seqMINER [75] and deeptools (-computeMatrix -skip0; -
844 plotHeatmap) with K-Means linear normalization. Genomic intersections and sequence extractions
845 were carried out using bedtools. GetFastaBed was used to extract FASTA sequences from BED files.
846 Intersect Interval and Multiple Intersect were applied to identify overlapping genomic locations.
847 WindowBed was utilized for gene-centric peak distribution analyses. When not specified, all
848 bioinformatics analyses were performed using default parameters, ensuring robust and reproducible
849 results.
850
851 **RNA extraction and analyses**
852 Total RNA from muscle tissue, LHCN-M2 and C79 cell lines was extracted using TRIzol reagent
853 (TRIREAGENT, Molecular Research Center, TR-118, 513-841-0900) as described [76]. RNA concentration
854 and purity were assessed spectrophotometrically using a NanoDrop system (Thermo Fisher Scientific).
855 For RNA isolation from FACS-isolated MuSC, the RNeasy Plus Micro Kit (Qiagen, 74034) was employed
856 according to the manufacturer's instructions.
857 For RT-qPCR experiments, 2 µg of total RNA underwent reverse transcription using SuperScript IV (Life
858 Technologies) with oligo(dT) primers, according to the supplier's protocol. cDNA was diluted hundred
859 times and quantitative PCR (qPCR) was performed with a Lightcycler 480 II (Roche) using the SYBR®
860 Green PCR kit (Roche), in accordance with the recommended protocol (2 µl cDNA, 4.8 µl H_2O, 5 µl
861 Syber Green 2x mix and 0.2 µl of 100 µM primer mix). The primer sequences for mouse and human
862 are detailed in Tables S5 and S6, respectively. Housekeeping genes *Tbp* (for mouse), and *HSP90AB1*
863 (for human) were used as internal controls. Data were analyzed using ΔΔCt [77] method.
864 For RNA sequencing (RNA-seq) and SMART-seq experiments, RNA integrity was assessed using a
865 Bioanalyzer. Library preparation was performed at the GenomEast platform from IGBMC.
866 For RNA-seq, cDNA library was prepared, and sequenced by the standard Illumina protocol (HiSeq
867 4000, single-end, 50 bp), following the manufacturer's instructions. Image analysis and base calling
868 were performed using RTA 2.7.7 and bcl2fastq 2.17.1.14. Adapter dimer reads were removed using
869 DimerRemover. FastQC 0.11.2 (http://www.bioinformatics.babraham.ac.uk/projects/fastqc/) was
870 used to evaluate the quality of the sequencing. Reads were mapped to the mouse mm10 genome
871 (NCBI Build 38) using STAR v2.7.10b [78]. Only uniquely aligned reads were retained for further analyses.

872 Quantification of gene expression was performed using HTSeq 0.11.0 [79]. For comparison among
873 datasets, the transcripts with more than 100 raw reads were considered.
874 For SMART-seq, full length cDNA was generated from 250 pg to 2 ng of total RNA using SMART-Seq®
875 mRNA Kit (Takara Bio Europe, Saint Germain en Laye, France), according to manufacturer's
876 instructions, with 12 cycles of PCR for cDNA amplification by Seq-Amp polymerase. Six hundred pg of
877 pre-amplified cDNA were used as input for Tn5 transposon tagmentation followed by 12 cycles of
878 library amplification using Nextera XT DNA Library Preparation Kit and IDT for Illumina DNA/RNA UD
879 Indexes, Tagmentation (Illumina, San Diego, USA). Following purification with SPRIselect beads
880 (Beckman-Coulter, Villepinte, France), the size and concentration of libraries were assessed using
881 Bioanalyzer 2100 system (Agilent technologies, Les Ulis, France). Libraries were sequenced on an
882 Illumina NextSeq 2000-X sequencer as paired-end 50 base reads. Image analysis and base calling were
883 performed using RTA version 2.7.7 and BCL Convert version 3.8.4. Adapter dimer reads were removed
884 with DimerRemover (-a AGATCGGAAGAGCACACGTCTGAACTCCAGTCAC), and the quality of
885 sequencing data was evaluated using FastQC 0.11.5. Reads were aligned to the mouse mm39 genome
886 using STAR v2.7.10b, retaining only uniquely mapped reads for downstream analyses. Gene expression
887 was quantified using STAR, and for dataset comparisons, only transcripts with more than 50 raw reads
888 were considered.
889 For RNA sequencing (RNA-seq) and SMART-seq experiments, differentially expressed genes (DEGs)
890 were identified using the Bioconductor libraries DESeq2 [80] with a $p < 0.05$. Identified DEGs were
891 subjected to functional analysis using STRING 12.0 [81] and to pathway analysis using WebGestalt [82] with
892 the Over-Representation Analysis (ORA) method, applying a false discovery rate (FDR) < 0.05 as the
893 significance threshold. Heatmaps were generated by centering and normalizing expression values
894 using Cluster 3.0 [83], with subsequent visualization Morpheus
895 (https://software.broadinstitute.org/morpheus/). Genes were clustered using K-Mean with gene tree
896 construction, Pearson correlation, and average linkage as clustering parameters [84].
897

898 **Single-cell RNA sequencing**

899 Single-cell RNA sequencing (scRNA-seq) experiments were performed on TA muscle cells, isolated
900 from 3 control ($AR^{L2/Y}$) and 3 $AR^{(i)sat-/Y}/YFP^{Tg/0}$ injured TA muscles at 5 dpi. TA muscles were dissociated
901 into single cells, as described above. Cells from each genotype group were pooled and stained with
902 DAPI, and DAPI-negative living cells were isolated using a BD FACS Aria™ Fusion flow cytometer. To
903 assess cell viability and yield, a Trypan blue exclusion assay was performed using a Neubauer Chamber.
904 Only samples with a viability greater than 95% were processed using a Chromium Controller (10X
905 Genomics, Leiden, The Netherlands). 16,500 total cells were loaded per well to yield approximately

906 10,000 captured cells into nanoliter-scale Gel Beads-in-Emulsion (GEMs). Single cell 3 prime mRNA seq
907 library were generated using Chromium Next GEM Single Cell 3 prime Reagent Kits v3.1 (10X
908 Genomics). Libraries were quantified and controlled for their quality using Bioanalyzer 2100 (Agilent
909 Technologies, Santa Clara CA), and further sequenced on an Illumina NextSeq 550 sequencer as
910 paired-end 28 + 100 base reads. Image analysis and base calling were performed using RTA version
911 2.7.7 [85] and Cell Ranger version 3.0.2 [86].
912 Data were processed using the Cell Ranger 7.0.0 count pipeline (10x Genomics) for read alignment,
913 barcode and unique molecular identifier (UMI) filtering, and gene quantification. A custom reference
914 genome was generated using the mkref function with the GRCm39 assembly of the *Mus musculus*
915 genome and Ensembl release 107 annotations. The output gene-barcode matrix was imported into
916 RStudio (version 2025.05.1) using the Read10X function from the Seurat package (version 5), yielding
917 a sparse matrix of UMI counts per gene per cell. Downstream analyses were conducted in RStudio
918 following standard Seurat v5 workflows [87], including quality control, normalization, dimensionality
919 reduction, clustering, and differential gene expression. For quality control, cells with <10%
920 mitochondrial content, <50% ribosomal gene expression, and total RNA features between 200 and
921 6000 were retained. Principal Component Analysis (PCA, dim=16) was used for dimensionality
922 reduction, and clustering was performed using a resolution parameter of 0.6. Differential gene
923 expression and further downstream analyses were conducted. Satellite cell reclustering was
924 performed with dimension reduction of 14 and cluster resolution of 0.3.
925 Cell-cell communication analysis was conducted using the CellChat R package within the RStudio
926 environment [88]. Normalized scRNA-seq data were used, and overexpressed ligands and receptors
927 were identified to infer intercellular signaling networks. Communication probabilities were computed
928 using the trimean method, with a minimum gene expression threshold of 0.1, and genes were
929 considered only if expressed in more than 10% of cells in the described groups. The CellChatDB ligand-
930 receptor interaction database was used as the reference. The analysis pipeline included identification
931 of major signaling inputs and outputs, classification of signaling roles (incoming, outgoing, mediator,
932 and influencer), and visualization via circle plots and hierarchical clustering. Inter-condition
933 comparisons were performed using the compareInteractions and rankNet functions. All analyses were
934 performed using default CellChat parameters, including 500 permutations for significance testing and
935 standard visualization settings, unless otherwise specified. Results were visualized and further
936 interpreted using built-in and custom R scripts. Cell cycle bioinformatic analyses were performed using
937 Scanpy function (scanpy.tl.score_genes_cell_cycle), with marker genes extracted from scRNA-seq of
938 mouse embryonic stem cells generated for DeepCycle as described [87, 89].
939

940 **Protein analysis**

941 TA muscles were mechanically ground in RIPA buffer [50 mM Tris (pH 7.5), 1% NP-40, 0.5% sodium
942 deoxycholate, 0.1% SDS, 150 mM NaCl, 5 mM EDTA, and a protease inhibitor cocktail (45 mg/ml;
943 Roche, Cat. No. 11 873 580 001)] at 4 °C. Alternatively, adherent cells were harvested in RIPA buffer,
944 and kept on ice for 10 min. TA muscles and cell lysates were centrifuged at 12,000 g for 10 minutes at
945 4 °C, and the supernatants were collected for further analysis. For western blot analyses,
946 homogenates were separated in 8% polyacrylamide gels, transferred to Hybond nitrocellulose
947 membranes (Amersham Biosciences), and probed with specific antibodies targeting AR (Abcam,
948 ab108341, 1:500), α-TUBULIN (IGBMC, 1Tub2A2, 1:5000), and GAPDH (Cell Signaling, #2118, 1:5000).
949 Secondary antibodies conjugated to horseradish peroxidase (anit-Mouse-HPR, Cell Signalling, 7076S,
950 1:10,000; anit-Rabbit-HPR, Cell Signalling, 7074S, 1:10,000;) were detected using chemiluminescence
951 detection systems (GE Healthcare, Amersham, ImageQuant 800 or Imager 600). Protein quantification
952 was assessed by the FIJI/ImageJ distribution software (https://imagej.net/ImageJ) [90].

953

954 **Statistical analyses**

955 Data processing and analysis were conducted using DESeq2, Microsoft Excel and GraphPad Prism 9. In
956 all graphical representations, error bars indicate the standard error mean (SEM). Comparisons
957 between groups were performed using appropriate statistical tests, selected based on the number of
958 groups, data distribution (normality), variance homogeneity, and multiple comparisons. The specific
959 statistical tests applied are indicated in the figure legends. Statistical significance was defined as
960 follows: ns, $p > 0.05$ (non-significant); *, $p < 0.05$; **, $p < 0.01$; and ***, $p < 0.001$.

961

962 **Data availability**

963 Custom macro for CSA measurements and Sirius Red quantification are available on GitLab and
964 GitHub, respectively (CSA: the BIOP cellpose extension guide; Sirius Red: https://github.com/Hugues-
965 Jacobs/Fibrosis_analysis). All sequencing datasets generated in this study have been deposited in the
966 Gene Expression Omnibus (GEO) under the following accession numbers: GSE303611 for single-cell
967 RNA-seq (token: afmhqcmenpapfyl), GSE303612 for SMART-seq (token: slileymohzanlal), GSE303614
968 for bulk RNA-seq (token: chqloqugddwjvur), GSE303615 for CUT&RUN analysis at 5 dpi (token:
969 gtovmecctvyprot), GSE303618 for CUT&RUN analysis at 7 dpi (token: ynahwacgxtotdct), and
970 GSE303620 for CUT&RUN analysis in non-injured animals (token: mjufuemerzyhlwn).

971 **REFERENCES**

972 1. Charge, S.B. & Rudnicki, M.A. Cellular and molecular regulation of muscle regeneration.
973 *Physiol Rev* **84**, 209-238 (2004).
974 2. Goel, A.J., Rieder, M.K., Arnold, H.H., Radice, G.L. & Krauss, R.S. Niche Cadherins Control the
975 Quiescence-to-Activation Transition in Muscle Stem Cells. *Cell Rep* **21**, 2236-2250 (2017).
976 3. Rozo, M., Li, L. & Fan, C.M. Targeting beta1-integrin signaling enhances regeneration in aged
977 and dystrophic muscle in mice. *Nat Med* **22**, 889-896 (2016).
978 4. Seale, P. *et al.* Pax7 is required for the specification of myogenic satellite cells. *Cell* **102**, 777-
979 786 (2000).
980 5. Wang, Y.X. & Rudnicki, M.A. Satellite cells, the engines of muscle repair. *Nat Rev Mol Cell Biol*
981 **13**, 127-133 (2011).
982 6. Anderson, J.E. Key concepts in muscle regeneration: muscle "cellular ecology" integrates a
983 gestalt of cellular cross-talk, motility, and activity to remodel structure and restore function.
984 *Eur J Appl Physiol* **122**, 273-300 (2022).
985 7. Zhang, W., Liu, Y. & Zhang, H. Extracellular matrix: an important regulator of cell functions and
986 skeletal muscle development. *Cell Biosci* **11**, 65 (2021).
987 8. Koike, H., Manabe, I. & Oishi, Y. Mechanisms of cooperative cell-cell interactions in skeletal
988 muscle regeneration. *Inflamm Regen* **42**, 48 (2022).
989 9. Abou-Khalil, R. *et al.* Autocrine and paracrine angiopoietin 1/Tie-2 signaling promotes muscle
990 satellite cell self-renewal. *Cell Stem Cell* **5**, 298-309 (2009).
991 10. Kedlian, V.R. *et al.* Human skeletal muscle aging atlas. *Nat Aging* **4**, 727-744 (2024).
992 11. Su, J. *et al.* A novel atlas of gene expression in human skeletal muscle reveals molecular
993 changes associated with aging. *Skelet Muscle* **5**, 35 (2015).
994 12. Moiseeva, V. *et al.* Senescence atlas reveals an aged-like inflamed niche that blunts muscle
995 regeneration. *Nature* **613**, 169-178 (2023).
996 13. Day, K., Shefer, G., Shearer, A. & Yablonka-Reuveni, Z. The depletion of skeletal muscle
997 satellite cells with age is concomitant with reduced capacity of single progenitors to produce
998 reserve progeny. *Dev Biol* **340**, 330-343 (2010).
999 14. Petermann-Rocha, F. *et al.* Global prevalence of sarcopenia and severe sarcopenia: a
1000 systematic review and meta-analysis. *J Cachexia Sarcopenia Muscle* **13**, 86-99 (2022).
1001 15. Munoz-Canoves, P., Neves, J. & Sousa-Victor, P. Understanding muscle regenerative decline
1002 with aging: new approaches to bring back youthfulness to aged stem cells. *FEBS J* **287**, 406-
1003 416 (2020).
1004 16. Rizk, J., Sahu, R. & Duteil, D. An overview on androgen-mediated actions in skeletal muscle
1005 and adipose tissue. *Steroids* **199**, 109306 (2023).
1006 17. Conboy, I.M. & Rando, T.A. The regulation of Notch signaling controls satellite cell activation
1007 and cell fate determination in postnatal myogenesis. *Dev Cell* **3**, 397-409 (2002).
1008 18. Seo, J.Y., Kim, J.H. & Kong, Y.Y. Unraveling the Paradoxical Action of Androgens on Muscle
1009 Stem Cells. *Mol Cells* **42**, 97-103 (2019).
1010 19. Niel, L., Willemsen, K.R., Volante, S.N. & Monks, D.A. Sexual dimorphism and androgen
1011 regulation of satellite cell population in differentiating rat levator ani muscle. *Dev Neurobiol*
1012 **68**, 115-122 (2008).
1013 20. Diel, P., Baadners, D., Schlupmann, K., Velders, M. & Schwarz, J.P. C2C12 myoblastoma cell
1014 differentiation and proliferation is stimulated by androgens and associated with a modulation
1015 of myostatin and Pax7 expression. *J Mol Endocrinol* **40**, 231-241 (2008).
1016 21. Chen, Y., Zajac, J.D. & MacLean, H.E. Androgen regulation of satellite cell function. *J Endocrinol*
1017 **186**, 21-31 (2005).
1018 22. Klose, A. *et al.* Castration induces satellite cell activation that contributes to skeletal muscle
1019 maintenance. *JCSM Rapid Commun* **1** (2018).
1020 23. Sakai, H. & Imai, Y. Cell-specific functions of androgen receptor in skeletal muscles. *Endocr J*
1021 **71**, 437-445 (2024).

1022 24. Sinha-Hikim, I., Taylor, W.E., Gonzalez-Cadavid, N.F., Zheng, W. & Bhasin, S. Androgen
1023 receptor in human skeletal muscle and cultured muscle satellite cells: up-regulation by
1024 androgen treatment. *J Clin Endocrinol Metab* **89**, 5245-5255 (2004).
1025 25. Ghaibour, K. *et al.* Androgen receptor coordinates muscle metabolic and contractile functions.
1026 *J Cachexia Sarcopenia Muscle* **14**, 1707-1720 (2023).
1027 26. Chambon, C. *et al.* Myocytic androgen receptor controls the strength but not the mass of limb
1028 muscles. *Proc Natl Acad Sci U S A* **107**, 14327-14332 (2010).
1029 27. Mourikis, P. & Tajbakhsh, S. Distinct contextual roles for Notch signalling in skeletal muscle
1030 stem cells. *BMC Dev Biol* **14**, 2 (2014).
1031 28. Pizza, F.X. & Buckley, K.H. Regenerating Myofibers after an Acute Muscle Injury: What Do We
1032 Really Know about Them? *Int J Mol Sci* **24** (2023).
1033 29. Oprescu, S.N., Yue, F., Qiu, J., Brito, L.F. & Kuang, S. Temporal Dynamics and Heterogeneity of
1034 Cell Populations during Skeletal Muscle Regeneration. *iScience* **23**, 100993 (2020).
1035 30. McKellar, D.W. *et al.* Large-scale integration of single-cell transcriptomic data captures
1036 transitional progenitor states in mouse skeletal muscle regeneration. *Commun Biol* **4**, 1280
1037 (2021).
1038 31. Yue, F. *et al.* Lipid droplet dynamics regulate adult muscle stem cell fate. *Cell Rep* **38**, 110267
1039 (2022).
1040 32. Morroni, J. *et al.* Injury-experienced satellite cells retain long-term enhanced regenerative
1041 capacity. *Stem Cell Res Ther* **14**, 246 (2023).
1042 33. Brun, C.E. *et al.* GLI3 regulates muscle stem cell entry into G(Alert) and self-renewal. *Nat*
1043 *Commun* **13**, 3961 (2022).
1044 34. Barsky, S.T. & Monks, D.A. The role of androgens and global and tissue-specific androgen
1045 receptor expression on body composition, exercise adaptation, and performance. *Biol Sex*
1046 *Differ* **16**, 28 (2025).
1047 35. Chinvattanachot, G., Rivas, D. & Duque, G. Mechanisms of muscle cells alterations and
1048 regeneration decline during aging. *Ageing Res Rev* **102**, 102589 (2024).
1049 36. Serra, C. *et al.* Testosterone improves the regeneration of old and young mouse skeletal
1050 muscle. *J Gerontol A Biol Sci Med Sci* **68**, 17-26 (2013).
1051 37. Oura, M. *et al.* Testosterone/androgen receptor antagonizes immobility-induced muscle
1052 atrophy through Inhibition of myostatin transcription and inflammation in mice. *Sci Rep* **15**,
1053 10568 (2025).
1054 38. Lai, Y. *et al.* Multimodal cell atlas of the ageing human skeletal muscle. *Nature* **629**, 154-164
1055 (2024).
1056 39. Tan, M.H., Li, J., Xu, H.E., Melcher, K. & Yong, E.L. Androgen receptor: structure, role in
1057 prostate cancer and drug discovery. *Acta Pharmacol Sin* **36**, 3-23 (2015).
1058 40. Gruntmanis, U. The Role of 5α-Reductase Inhibition in Men Receiving Testosterone
1059 Replacement Therapy. *JAMA* **307**, 968-970 (2012).
1060 41. Bartsch, G., Rittmaster, R.S. & Klocker, H. Dihydrotestosterone and the concept of 5alpha-
1061 reductase inhibition in human benign prostatic hyperplasia. *Eur Urol* **37**, 367-380 (2000).
1062 42. Dubois, V., Laurent, M., Boonen, S., Vanderschueren, D. & Claessens, F. Androgens and
1063 skeletal muscle: cellular and molecular action mechanisms underlying the anabolic actions.
1064 *Cell Mol Life Sci* **69**, 1651-1667 (2012).
1065 43. Sheppard, R.L., Spangenburg, E.E., Chin, E.R. & Roth, S.M. Androgen receptor polyglutamine
1066 repeat length affects receptor activity and C2C12 cell development. *Physiol Genomics* **43**,
1067 1135-1143 (2011).
1068 44. Fu, S., Lin, X., Yin, L. & Wang, X. Androgen receptor regulates the proliferation of myoblasts
1069 under appropriate or excessive stretch through IGF-1 receptor mediated p38 and ERK1/2
1070 pathways. *Nutr Metab (Lond)* **18**, 85 (2021).

1071 45. Fu, S., Hu, J., Wang, G., Qian, Z. & Wang, X. Androgen receptor regulates the differentiation of
1072 myoblasts under cyclic mechanical stretch and its upstream and downstream signals. *Int J Biol*
1073 *Macromol* **281**, 136257 (2024).
1074 46. Dubois, V. *et al.* Androgen Deficiency Exacerbates High-Fat Diet-Induced Metabolic Alterations
1075 in Male Mice. *Endocrinology* **157**, 648-665 (2016).
1076 47. Rocchi, A. *et al.* Glycolytic-to-oxidative fiber-type switch and mTOR signaling activation are
1077 early-onset features of SBMA muscle modified by high-fat diet. *Acta Neuropathol* **132**, 127-
1078 144 (2016).
1079 48. Campbell, M.D., Djukovic, D., Raftery, D. & Marcinek, D.J. Age-related changes of skeletal
1080 muscle metabolic response to contraction are also sex-dependent. *J Physiol* **603**, 69-86 (2025).
1081 49. Grevendonk, L. *et al.* Impact of aging and exercise on skeletal muscle mitochondrial capacity,
1082 energy metabolism, and physical function. *Nat Commun* **12**, 4773 (2021).
1083 50. Kobayashi, A., Azuma, K., Ikeda, K. & Inoue, S. Mechanisms Underlying the Regulation of
1084 Mitochondrial Respiratory Chain Complexes by Nuclear Steroid Receptors. *Int J Mol Sci* **21**
1085 (2020).
1086 51. Jomova, K. *et al.* Reactive oxygen species, toxicity, oxidative stress, and antioxidants: chronic
1087 diseases and aging. *Arch Toxicol* **97**, 2499-2574 (2023).
1088 52. Lee, J. *et al.* Androgen Deprivation Therapy-Induced Muscle Loss and Fat Gain Predict
1089 Cardiovascular Events in Prostate Cancer Patients. *J Cachexia Sarcopenia Muscle* **16**, e13844
1090 (2025).
1091 53. Argiles, J.M., Campos, N., Lopez-Pedrosa, J.M., Rueda, R. & Rodriguez-Manas, L. Skeletal
1092 Muscle Regulates Metabolism via Interorgan Crosstalk: Roles in Health and Disease. *J Am Med*
1093 *Dir Assoc* **17**, 789-796 (2016).
1094 54. Penvose, A., Keenan, J.L., Bray, D., Ramlall, V. & Siggers, T. Comprehensive study of nuclear
1095 receptor DNA binding provides a revised framework for understanding receptor specificity.
1096 *Nat Commun* **10**, 2514 (2019).
1097 55. Gelman, L. *et al.* Integrating nuclear receptor mobility in models of gene regulation. *Nucl*
1098 *Recept Signal* **4**, e010 (2006).
1099 56. Hager, G.L., Nagaich, A.K., Johnson, T.A., Walker, D.A. & John, S. Dynamics of nuclear receptor
1100 movement and transcription. *Biochim Biophys Acta* **1677**, 46-51 (2004).
1101 57. Stavreva, D.A. *et al.* Nuclear Receptors Dynamics and Gene Regulation in Response to
1102 Ultradian Hormone Pulses. *Endocrinology* **166**, bqaf043.034 (2025).
1103 58. Forouhan, M. *et al.* AR cooperates with SMAD4 to maintain skeletal muscle homeostasis. *Acta*
1104 *Neuropathol* **143**, 713-731 (2022).
1105 59. Nath, S.R. *et al.* Androgen receptor polyglutamine expansion drives age-dependent quality
1106 control defects and muscle dysfunction. *J Clin Invest* **128**, 3630-3641 (2018).
1107 60. Arnold, F.J., Pluciennik, A. & Merry, D.E. Impaired Nuclear Export of Polyglutamine-Expanded
1108 Androgen Receptor in Spinal and Bulbar Muscular Atrophy. *Sci Rep* **9**, 119 (2019).
1109 61. Shiina, H. *et al.* Premature ovarian failure in androgen receptor-deficient mice. *Proc Natl Acad*
1110 *Sci U S A* **103**, 224-229 (2006).
1111 62. Murphy, M.M., Lawson, J.A., Mathew, S.J., Hutcheson, D.A. & Kardon, G. Satellite cells,
1112 connective tissue fibroblasts and their interactions are crucial for muscle regeneration.
1113 *Development* **138**, 3625-3637 (2011).
1114 63. Tosic, M. *et al.* Lsd1 regulates skeletal muscle regeneration and directs the fate of satellite
1115 cells. *Nat Commun* **9**, 366 (2018).
1116 64. Chenu, C. *et al.* Testosterone Prevents Cutaneous Ischemia and Necrosis in Males Through
1117 Complementary Estrogenic and Androgenic Actions. *Arterioscler Thromb Vasc Biol* **37**, 909-
1118 919 (2017).
1119 65. Rovito, D. *et al.* Myod1 and GR coordinate myofiber-specific transcriptional enhancers. *Nucleic*
1120 *Acids Res* **49**, 4472-4492 (2021).

1121 66. Simon, A. *et al.* Transcriptomic characterization of postnatal muscle maturation. *Dis Model*
1122 *Mech* **18** (2025).
1123 67. Cigrang, M. *et al.* Pan-inhibition of super-enhancer-driven oncogenic transcription by next-
1124 generation synthetic ecteinascidins yields potent anti-cancer activity. *Nat Commun* **16**, 512
1125 (2025).
1126 68. Ghaibour, K. *et al.* An Efficient Protocol for CUT&RUN Analysis of FACS-Isolated Mouse
1127 Satellite Cells. *J Vis Exp* (2023).
1128 69. Janssens, D.H. *et al.* Automated in situ chromatin profiling efficiently resolves cell types and
1129 gene regulatory programs. *Epigenetics Chromatin* **11**, 74 (2018).
1130 70. Langmead, B. & Salzberg, S.L. Fast gapped-read alignment with Bowtie 2. *Nat Methods* **9**, 357-
1131 359 (2012).
1132 71. Ramirez, F., Dundar, F., Diehl, S., Gruning, B.A. & Manke, T. deepTools: a flexible platform for
1133 exploring deep-sequencing data. *Nucleic Acids Res* **42**, W187-191 (2014).
1134 72. Quinlan, A.R. & Hall, I.M. BEDTools: a flexible suite of utilities for comparing genomic features.
1135 *Bioinformatics* **26**, 841-842 (2010).
1136 73. Meers, M.P., Tenenbaum, D. & Henikoff, S. Peak calling by Sparse Enrichment Analysis for
1137 CUT&RUN chromatin profiling. *Epigenetics Chromatin* **12**, 42 (2019).
1138 74. Zhang, Y. *et al.* Model-based analysis of ChIP-Seq (MACS). *Genome Biol* **9**, R137 (2008).
1139 75. Ye, T. *et al.* seqMINER: an integrated ChIP-seq data interpretation platform. *Nucleic Acids Res*
1140 **39**, e35 (2011).
1141 76. Cai, Q. *et al.* LSD1 inhibition circumvents glucocorticoid-induced muscle wasting of male mice.
1142 *Nat Commun* **15**, 3563 (2024).
1143 77. Livak, K.J. & Schmittgen, T.D. Analysis of relative gene expression data using real-time
1144 quantitative PCR and the 2(-Delta Delta C(T)) Method. *Methods* **25**, 402-408 (2001).
1145 78. Dobin, A. *et al.* STAR: ultrafast universal RNA-seq aligner. *Bioinformatics* **29**, 15-21 (2013).
1146 79. Anders, S., Pyl, P.T. & Huber, W. HTSeq--a Python framework to work with high-throughput
1147 sequencing data. *Bioinformatics* **31**, 166-169 (2015).
1148 80. Love, M.I., Huber, W. & Anders, S. Moderated estimation of fold change and dispersion for
1149 RNA-seq data with DESeq2. *Genome Biol* **15**, 550 (2014).
1150 81. Szklarczyk, D. *et al.* The STRING database in 2023: protein-protein association networks and
1151 functional enrichment analyses for any sequenced genome of interest. *Nucleic Acids Res* **51**,
1152 D638-D646 (2023).
1153 82. Wang, J., Duncan, D., Shi, Z. & Zhang, B. WEB-based GEne SeT AnaLysis Toolkit (WebGestalt):
1154 update 2013. *Nucleic Acids Res* **41**, W77-83 (2013).
1155 83. de Hoon, M.J., Imoto, S., Nolan, J. & Miyano, S. Open source clustering software.
1156 *Bioinformatics* **20**, 1453-1454 (2004).
1157 84. Lu, Y., Lu, S., Fotouhi, F., Deng, Y. & Brown, S.J. Incremental genetic K-means algorithm and its
1158 application in gene expression data analysis. *BMC Bioinformatics* **5**, 172 (2004).
1159 85. Raine, A., Liljedahl, U. & Nordlund, J. Data quality of whole genome bisulfite sequencing on
1160 Illumina platforms. *PLoS One* **13**, e0195972 (2018).
1161 86. Lun, A.T.L. *et al.* EmptyDrops: distinguishing cells from empty droplets in droplet-based single-
1162 cell RNA sequencing data. *Genome Biol* **20**, 63 (2019).
1163 87. Satija, R., Farrell, J.A., Gennert, D., Schier, A.F. & Regev, A. Spatial reconstruction of single-cell
1164 gene expression data. *Nat Biotechnol* **33**, 495-502 (2015).
1165 88. Jin, S. *et al.* Inference and analysis of cell-cell communication using CellChat. *Nat Commun* **12**,
1166 1088 (2021).
1167 89. Riba, A. *et al.* Cell cycle gene regulation dynamics revealed by RNA velocity and deep-learning.
1168 *Nat Commun* **13**, 2865 (2022).
1169 90. Schneider, C.A., Rasband, W.S. & Eliceiri, K.W. NIH Image to ImageJ: 25 years of image analysis.
1170 *Nat Methods* **9**, 671-675 (2012).

1171

1172 **ACKNOWLEDGMENTS**

1173 We thank Dr. J. Laporte (IGBMC) for generously providing the LHCN-M2 and C79 cell lines. We are
1174 grateful to Anastasia Bannwarth, Nikola Djordjevic, and Régis Lutzing for their valuable technical
1175 support, and Valentine Gilbart, Tao Ye and Céline Keime for excellent bioinformatics assistance. We
1176 extend our gratitude to Mohammed Selloum and Aurélie Aubertin for their valuable scientific
1177 expertise on biochemical analyses. We are grateful to Prof. S. Kato for providing the AR floxed mice,
1178 and Prof. G. Kardon for the *Pax7*-CreER^{T2} line. We acknowledge the support of the IGBMC core
1179 facilities, including the animal facility, microscopy and electron microscopy platforms, biochemistry,
1180 cell culture service, flow cytometry, and histopathology services, as well as the Mouse Clinical Institute
1181 (ICS, Illkirch-Graffenstaden, France) and GenomEast facility, a member of the 'France Génomique'
1182 consortium (ANR-10-INBS-0009).

1183 This work was supported by the Interdisciplinary Thematic Institute IMCBio as part of the ITI 2021-
1184 2028 program of the University of Strasbourg, the Centre National pour la Recherche Scientifique
1185 (CNRS), Institut national de la santé et de la recherche médicale (Inserm), from IdEx Unistra (ANR-10-
1186 IDEX-0002), SFRI-STRAT'US (ANR 20-SFRI-0012) and EUR IMCBio (ANR-17-EURE-0023) projects, under
1187 the framework of the French Investments for the Future Programme. Additional support was provided
1188 by Inserm, CNRS, Unistra, IGBMC, AFM-Téléthon (grant application #24376), and the Agence Nationale
1189 de la Recherche (ANR-10-BLAN-1108, ANR-24-CE14-0247-01). J.G.R. received funding from the
1190 Programme CDFA-07-22 from the Université franco-allemande and Ministère de l'Enseignement
1191 Supérieur de la Recherche et de l'Innovation. K.C.G. received funding by the Association pour la
1192 Recherche à l'IGBMC (ARI), E.C by MESRI, Q.C by ANR (ANDROMETAMUS, ANR-24-CE14-0247-01), and
1193 R.S. by IMCBio. Anastasia Bannwarth received funding from AFM-Téléthon (grant application #24376)
1194 for technical assistance.

1195

1196 **AUTHOR CONTRIBUTIONS**

1197 D.D., J.G.R., and K.C.G. formulated the initial hypothesis. J.G.R., K.C.G., S.S.C., A.B., Q.C., G. R., E.C., and
1198 R.S. carried out functional, molecular, and histological experiments. D.D., J.G.R., N.M., and G.Z.
1199 executed bioinformatics analyses. J.G.R., N.M., H.J., and E.G. took responsibility of imaging analyses.
1200 A.F. conducted *in situ* myofiber contraction experiments. J-F.A. and C.F. provided DHT pellets and
1201 performed initial *in vivo* tests. J.G.R., K.C.G., D.M., and D.D. took primary responsibility for data
1202 analysis and writing the manuscript.

1203

1204 **Declaration of interests**

1205 The authors declare no competing interests.

ETHICS DECLARATIONS

Competing interests

The authors declare no competing interests.

1209 **FIGURE LEGENDS**

1210 **Figure 1: Absence of MuSC-AR impairs muscle regenerative capacities at young age.**

1211 **(A)** Representative hematoxylin and eosin (H&E) staining of tibialis anterior (TA) muscles of young
1212 control and $AR^{(i)sat-/Y}$ male mice under non-injured (NI) condition, and at 7 days post-injury (7 dpi).
1213 Black arrows indicate centrally nucleated fibers. Cyan arrows point to immune infiltration. Yellow
1214 arrows denote necrotic fibers. Green arrows show interstitial space. Pink arrows label misshaped
1215 regenerating myofibers. Orange arrows mark fibrosis. Scale bars, 75 µm.

1216 **(B)** Ultrastructure analysis of NI and 7-days-injured TA of young control and $AR^{(i)sat-/Y}$ male mice. Z: Z-
1217 line, M: M-line, I: I-bands, A: A-band. Black arrows indicate M-line disturbances. Red arrows point to
1218 Z-line disruption. Pink arrows depict T-tubules misalignments. Orange arrows denote fibrosis. Green
1219 arrows show the A-band placement. Yellow arrows label the I-bands placements. Scale bars, 1 µm.

1220 **(C)** Distribution of myofibers cross-section area (CSA) in TA muscles of young control and $AR^{(i)sat-/Y}$ male
1221 mice 7 dpi. Data are presented as mean ± SEM. Statistical test used Two-way ANOVA with Sidak's
1222 correction; * = $p < 0.05$; ** = $p < 0.01$.

1223 **(D)** *In situ* single-fiber isometric force of 28-days-injured TA of young control and $AR^{(i)sat-/Y}$ male mice.
1224 Data are presented as mean ± SEM. Statistical test used was two-tailed Mann-Whitney test; * = $p <$
1225 0.05.

1226 **(E-F)** Representative immunofluorescent labeling of PAX7 (in red) **(E)**, and corresponding
1227 quantification of the number of PAX7-positive cells **(F)**, in 7-days-injured TA of young control and
1228 $AR^{(i)sat-/Y}$ male mice. White arrows point to PAX7-positive cells. Nuclei were stained with DAPI. Data are
1229 presented as mean ± SEM. Statistical test used is two-tailed Mann-Whitney test; ** = $p < 0.01$.

1230 **(G-H)** Heatmap depicting the mean centered normalized expression of indicated genes selected from
1231 bulk RNA-sequencing analysis performed in 7-days-injured TA of young control and $AR^{(i)sat-/Y}$ male mice
1232 **(G)**, and corresponding pathway analysis **(H)**.

1233 **(I)** Violin plots representing the normalized read counts of the indicated genes, selected from bulk
1234 RNA-sequencing analysis performed in 7-days-injured TA of young control and $AR^{(i)sat-/Y}$ male mice.
1235 Statistical test used is Wald test; ** = $p < 0.01$; *** = $p < 0.001$.

1236 **(J)** Representative immunofluorescent detection of DMD (in red), in 7-days-injured TA of young
1237 control and $AR^{(i)sat-/Y}$ male mice. Nuclei were stained with DAPI. White arrows depict fibers emerging
1238 within other fibers. Scale bars, 100 µm.

1239 **(K)** Representative immunofluorescent detection of DMD (in red), and sarcomeric alpha actinin
1240 (ACTN1) (in green), in 7-days-injured transversal and longitudinal sections of TA of young control and
1241 $AR^{(i)sat-/Y}$ male mice. Nuclei were stained with DAPI. White arrows point to nuclei. Yellow arrows denote

1242 sarcolemma discontinuation. Red arrows show ACTN1 aggregates. Pink arrows denote stairs-shape in
1243 regenerating fibers. Scale bars, 50 µm.
1244 **(L-M)** Representative immunofluorescent detection of embryonic myosin (MYH3) (in green), and
1245 LAMA2 (in magenta) **(L)**, and corresponding quantification of the number of MYH3-positive cells **(M)**
1246 in 5- and 7-days-injured TA of young control and $AR^{(i)sat-/Y}$ male mice. Nuclei were stained with DAPI.
1247 Scale bars, 85 µm. Data are presented as mean ± SEM. Statistical test used is Two-way ANOVA with
1248 Tukey correction; ns, non-significant; ** = $p < 0.01$; *** = $p < 0.001$.
1249 **(N-O)** Violin plots representing the normalized read counts of the indicated genes encoding myosin
1250 heavy chain (*Myh*s) isoforms **(N)**, or subunits of the electron transport chain complexes **(O)** selected
1251 from bulk RNA-sequencing analysis performed in 7-days-injured TA of young control and $AR^{(i)sat-/Y}$ male
1252 mice. Statistical test used is Wald test; * = $p < 0.05$; ** = $p < 0.01$; *** = $p < 0.001$.
1253 **(P)** Representative histochemical staining of NADH dehydrogenase (NADH-DH) and COX activities in
1254 7-days-injured TA of young control and $AR^{(i)sat-/Y}$ male mice. Oxidative and intermediate fibers are
1255 darkly and moderately stained, respectively; glycolytic fibers are lightly stained. Scale bars, 200 µm.
1256 **(Q)** Mitochondrial respiration profile of vehicle and 100 nM flutamide-treated LHCN-M2 cells,
1257 assessed using the Seahorse Mito Stress Test, following sequential injection of oligomycin, carbonyl
1258 cyanide-p-trifluoromethoxyphenylhydrazone (FCCP), and rotenone/AA, and expressed as oxygen
1259 consumption rate (OCR). Data are normalized to total nuclear counts, and presented as mean ± SEM.
1260 Statistical test used was two-tailed Mann-Whitney test; * = $p < 0.05$.
1261
1262 **Figure 2: Characterization of AR cistrome and transcriptome in MuSC at young age.**
1263 **(A)** Heatmap depicting the mean centered normalized expression of indicated genes selected from
1264 bulk RNA-sequencing analysis performed in 7-days-injured TA of young control and $AR^{(i)sat-/Y}$ male mice.
1265 **(B)** Pathway analysis of down- and up-regulated genes in 7-days-injured TA of young control and
1266 $AR^{(i)sat-/Y}$ male mice.
1267 **(C-D)** Violin plots representing the normalized read counts of the indicated genes, selected from bulk
1268 RNA-sequencing analysis performed in 7-days-injured TA of young control and $AR^{(i)sat-/Y}$ male mice.
1269 Statistical test used is Wald test; * = $p < 0.05$; ** = $p < 0.01$; *** = $p < 0.001$.
1270 **(E)** HOMER known and *de novo* motif analyses of AR-bound DNA sequences from 7-day-injured TA of
1271 young male mice.
1272 **(F)** Pathway analysis performed on AR target genes identified by CUT&RUN in MuSC of 7-day-injured
1273 TA of young male mice. Pathways of interest are squared in red.
1274 **(G)** Cumulative number of down-regulated genes, and up-regulated genes in MuSC of 7-day-injured
1275 TA of young male mice, with an AR peak located at the indicated distances from their TSS.

1276 **(H)** AR localization at the *Ar*, *Fzd4*, *Kdmc4*, *Myh1*, *Tead1*, and *Mylk4* loci, with binding sites shown in
1277 red.
1278
1279 **Figure 3: MuSC microenvironment is altered in the absence of AR.**
1280 **(A-B)** Uniform manifold approximation and projection (UMAP) visualization of single cells **(A)**, and
1281 respective percentage of cell types **(B)**, from 5-days-injured control and $AR^{(i)sat-/Y}$ TA of young mice,
1282 colored by cluster identity.
1283 **(C-D)** Percentage of macrophages **(C)**, immune cells, FAPs and MuSC **(D)**, in 5-days-injured TA of young
1284 control and $AR^{(i)sat-/Y}$ mice, analyzed from flow-cytometry data conducted at the indicated time-point.
1285 Data are presented as mean ± SEM. Statistical test used was two-tailed Mann-Whitney test; ns, non-
1286 significant; * = $p < 0.05$, *** = $p < 0.001$.
1287 **(E)** Violin plot of *Ar* transcript levels in the indicated cell populations identified from 5-days-injured TA
1288 of young control and $AR^{(i)sat-/Y}$ mice.
1289 **(F)** Schematic diagram of cell-cell communication between MuSC and other TA constitutive cells types
1290 in 5-days-injured TA of young control and $AR^{(i)sat-/Y}$ mice. Arrow thickness indicates the relative
1291 interaction strength between populations, as inferred from ligand-receptor expression analysis.
1292 **(G-H)** Violin plots representing the transcript levels of macrophage type-1 **(G)**, and macrophage type-
1293 2 markers **(H)**, selected from scRNA-seq analysis performed in 5-days-injured TA of young control and
1294 $AR^{(i)sat-/Y}$ mice.
1295 **(I)** Percentage of immune cells, FAPs and MuSC, in 7-days-injured TA of young control and $AR^{(i)sat-/Y}$
1296 mice, analyzed from flow-cytometry data conducted at the indicated time-point. Data are presented
1297 as mean ± SEM. Statistical test used was two-tailed Mann-Whitney test; ns, non-significant; ** = $p <$
1298 0.01; *** = $p < 0.001$.
1299 **(J-K)** Representative immunofluorescent detection of F4/80 (in green) **(J)**, and corresponding
1300 quantification of mean fluorescence intensity (MFI) of F4/80 signal **(K)**, in 7-days-injured TA of young
1301 control and $AR^{(i)sat-/Y}$ mice. White arrows depict inter-fiber macrophages. Red arrows point to intra-
1302 fibers macrophages. Nuclei were stained with DAPI. Scale bars, 100 µm for the main, 30 µm for
1303 magnified inset. Statistical test used was two-tailed Mann-Whitney test; ns, non-significant.
1304 **(L)** Representative Sirius Red histochemical staining visualized under brightfield (upper panel), and
1305 polarized light (lower panel), in 7-days-injured TA of young control and $AR^{(i)sat-/Y}$ mice. Black arrows
1306 point to collagen fibers deposition. White arrows depict type I collagen fibers. Cyan blue arrows
1307 indicate type III collagen fibers. Scale bars, 250 µm for the main, 90 µm for magnified inset.

1308 **(M-N)** Quantification of Sirius Red area from brightfield analysis **(M)**, and fibrosis composition **(N)** of
1309 7-days-injured TA of young control and $AR^{(i)sat-/Y}$ mice. Data are presented as mean ± SEM. Statistical
1310 test used was two-tailed Mann-Whitney test; ns, non-significant; ** = $p < 0.01$.
1311 **(O-P)** Representative immunofluorescent detection of perilipin (PLIN1) (red) **(O)**, and corresponding
1312 quantification **(P)**, in 5- and 7-days-injured TA of young control and $AR^{(i)sat-/Y}$ mice. White arrows point
1313 to adipocytes. Nuclei were stained with DAPI. Scale bars, 100 µm. Data are presented as mean ± SEM.
1314 Statistical test used Two-way ANOVA with Sidak's correction; * = $p < 0.05$.
1315 **(Q)** Schematic overview of the influence of AR signaling in MuSC within the regenerative niche at
1316 young age. MuSC-AR contributes to the orchestration of the immune response during muscle
1317 regeneration by ensuring the timely coordination of pro- and anti-inflammatory phases. In parallel,
1318 MuSC-AR signaling restrains FAPs from excessive extracellular matrix deposition and adipogenic
1319 differentiation. Green arrows indicate activation, red arrows indicate inhibition, and black arrows
1320 represent undefined interactions.
1321
1322 **Figure 4: AR deficiency in MuSC favors symmetric differentiation over asymmetric division or**
1323 **symmetric self-renewal**
1324 **(A)** UMAP visualization of MuSC reclusters from 5-days-injured control and $AR^{(i)sat-/Y}$ TA of young mice,
1325 colored by cluster identity.
1326 **(B)** Violin plots representing the expression level of indicated genes in MuSC reclusters, selected from
1327 scRNA-seq analysis performed in 5-days-injured TA of young control and $AR^{(i)sat-/Y}$ mice.
1328 **(C)** Cell cycle distribution across MuSC reclusters in 5-days-injured TA of young control and $AR^{(i)sat-/Y}$
1329 mice, showing the proportion of cells in G1, S, and G2/M phases.
1330 **(D-F)** Representative immunofluorescent detection of PAX7 (magenta), and KI67 (green) **(D)**, and
1331 corresponding quantifications in 5- **(E)** and 7-days **(F)** injured TA of young control and $AR^{(i)sat-/Y}$ mice.
1332 Nuclei were stained with DAPI. Scale bars, 100 µm for the main, 30 µm for magnified inset. Statistical
1333 test used is Two-way ANOVA with Tukey correction; ns, non-significant; * = $p < 0.05$; *** = $p < 0.001$.
1334 **(G-I)** Representative immunofluorescent detection of PAX7 (magenta) and MYOG (green), and
1335 corresponding quantifications in 5- **(H)** and 7-days **(I)** injured TA of young control and $AR^{(i)sat-/Y}$ mice.
1336 Nuclei were stained with DAPI. Scale bars, 100 µm for the main, 30 µm for magnified inset. Data are
1337 presented as mean ± SEM. Statistical test used is Two-way ANOVA with Tukey correction; ns, non-
1338 significant; * = $p < 0.05$; *** = $p < 0.001$.
1339 **(J-K)** Representative immunofluorescent detection of MYOG (in magenta) and KI67 (in green) **(J)**, and
1340 corresponding quantification of the number of MYOG/KI67-double positive cells per field of injury **(K)**,
1341 in 5- and 7-days-injured TA of young control and $AR^{(i)sat-/Y}$ mice. White arrows depict MYOG/KI67-

1342 double positive cells. Nuclei were stained with DAPI. Scale bars, 75 µm for the main, 30 µm for
1343 magnified inset. Data are presented as mean ± SEM. Statistical test used is Two-way ANOVA with
1344 Tukey correction; ** = $p < 0.01$; *** = $p < 0.001$.
1345 **(L)** Representative HE staining of TA muscles of young control and $AR^{(i)sat-/Y}$ mice, 7 (single injury) and
1346 28+7 (double injury) days after injury. Cyan blue arrows denote inflammatory cells. Green arrows point
1347 to interstitial space. Black arrows depict central nuclei. Pink arrows show misshaped fibers. Scale bars,
1348 100 µm.
1349 **(M)** Representative immunofluorescent detection of DMD (red), and PAX7 (green), of 28+7-days-
1350 injured young control and $AR^{(i)sat-/Y}$ mouse TA. Scale bars, 50 µm.
1351 **(N)** Quantification of the number of PAX7-positive cells in 28+7-days-injured young control and $AR^{(i)sat-}$
1352 $^{/Y}$ mouse TA. Data are presented as mean ± SEM. Statistical test used was two-tailed Mann-Whitney
1353 test; * = $p < 0.05$.
1354 **(O)** Schematic overview of MuSC-autonomous regulation by AR signaling at young age. AR activity in
1355 MuSC promotes self-renewing divisions (maintenance plane), leading to the preservation of the stem
1356 cell pool. Conversely, AR signaling inhibits commitment divisions (commitment plane). Green arrow
1357 indicate activation, and red arrows indicate inhibition.
1358
1359 **Figure 5: MuSC-AR exhibits time-dependent binding to target genes following injury**
1360 **(A)** HOMER known and *de novo* motif analyses of AR-bound DNA sequences from 5-day-injured TA of
1361 young male mice.
1362 **(B)** Pathway analysis performed on AR common target genes identified in MuSC of 5-day-injured TA
1363 of young male mice.
1364 **(C-D)** Cumulative number of down-regulated genes **(C)**, and up-regulated genes **(D)** in MuSC of 5-day-
1365 injured TA of young male mice, with an AR peak located at the indicated distances from their TSS.
1366 **(E)** AR localization at the *Clock*, *Eif2d*, and *Psma4* loci. Binding sites are indicated in red.
1367 **(F)** Average tag density profiles, and corresponding tag density map of AR in NI, 5- and 7-days injured
1368 TA muscles of young male mice, +/− 2 kb from the AR peak center.
1369 **(G)** Overlap among genes bound by AR, in NI, 5- and 7-days injured TA muscles of young male mice.
1370 **(H)** AR localization in MuSC in NI, 5- and 7-days injured TA muscles of young male mice, at indicated
1371 loci.
1372 **(I)** Schematic overview of AR-mediated temporal regulation and chromatin binding dynamics in MuSC
1373 during regeneration at young age. AR displays stage-specific chromatin occupancy throughout muscle
1374 regeneration. In uninjured muscle, MuSC-AR supports homeostasis. Following injury, AR translocates

1375 to genomic regions that drive regenerative programs, favoring genes involved in MuSC activation and
1376 proliferation at 5 dpi, and shifting toward loci promoting differentiation and maturation by 7 dpi.
1377
1378 **Figure 6: Age-related androgen decline alters skeletal muscle repair machinery**
1379 **(A)** Serum testosterone levels of control male mice at indicated time-points (young, mid-old and old).
1380 Basal level is represented by a dashed line. Data are presented as mean ± SEM. Statistical test used is
1381 Ordinary One-way ANOVA relative to 2-month-old mice. ns, non-significant; * = $p < 0.05$; ** = $p < 0.01$.
1382 **(B)** Relative *Ar* transcript levels in TA muscles of control mice at indicated time-points (young, mid-old
1383 and old). Data are presented as mean ± SEM. Statistical test used is Ordinary One-way ANOVA. *** =
1384 $p < 0.001$.
1385 **(C-D)** Representative western blot analysis **(C)**, and corresponding quantification of the indicated
1386 proteins **(D)** in TA of young and old control male mice. GAPDH was used as a loading control. Data are
1387 presented as mean ± SEM. Statistical test used was two-tailed Mann-Whitney test; *** = $p < 0.001$.
1388 **(E)** Relative *Pax7* transcript levels in TA muscles from young and old control male mice. Data are
1389 presented as mean ± SEM. Statistical test used was two-tailed Mann-Whitney test; * = $p < 0.05$.
1390 **(F)** Representative hematoxylin and eosin (H&E) staining of TA muscles of control and $AR^{(i)sat-/Y}$ old
1391 male mice under non-injured (NI) condition, and at 7 dpi. Black arrows indicate centrally nucleated
1392 fibers. Blue arrows point to immune infiltration. Yellow arrows denote necrotic fibers. Green arrows
1393 show interstitial space. Pink arrows label misshaped regenerating myofibers. Orange arrows mark
1394 fibrosis. Scale bars, 75 µm.
1395 **(G)** Ultrastructure analysis of NI and 7-days-injured TA of control and $AR^{(i)sat-/Y}$ old male mice. Black
1396 arrows indicate M-line disturbances. Red arrows point to Z-line disruption. Pink arrows depict T-
1397 tubules misalignments. Orange arrows denote fibrosis. Green arrows show the A-band placement.
1398 Yellow arrows label the I-bands placements. Scale bars, 1 µm.
1399 **(H)** Representative immunofluorescent labeling of PAX7 (in red), and corresponding quantification of
1400 the number of PAX7-positive cells in 7-days-injured TA of control and $AR^{(i)sat-/Y}$ old male mice. White
1401 arrows point to PAX7-positive cells. Nuclei were stained with DAPI. Data are presented as mean ± SEM.
1402 Statistical test used is two-tailed Mann-Whitney test; * = $p < 0.05$.
1403 **(I)** Representative immunofluorescent detection of DMD (in red), in 7-days-injured TA of control and
1404 $AR^{(i)sat-/Y}$ old male mice. Nuclei were stained with DAPI. Scale bars, 100 µm.
1405 **(J)** Representative histochemical staining of NADH dehydrogenase (NADH-DH) and COX activities in 7-
1406 days-injured TA of control and $AR^{(i)sat-/Y}$ old male mice. Oxidative and intermediate fibers are darkly
1407 and moderately stained, respectively; glycolytic fibers are lightly stained. Scale bars, 200 µm.

1408 **(K)** Representative Sirius Red histochemical staining visualized under brightfield, and corresponding
1409 quantification of Sirius Red area, in 7-days-injured TA of control and $AR^{(i)sat-/Y}$ old male mice. Black
1410 arrows point to collagen fibers deposition. Scale bars, 250 µm. Data are presented as mean ± SEM.
1411 Statistical test used was two-tailed Mann-Whitney test; *** = p < 0.001.
1412 **(L)** Representative immunofluorescent detection of perilipin (PLIN1) (green), and corresponding
1413 quantification of total number of adipocytes, in 5- and 7-days-injured TA of control and $AR^{(i)sat-/Y}$ old
1414 mice. White arrows point to adipocytes. Nuclei were stained with DAPI. Scale bars, 100 µm. Data are
1415 presented as mean ± SEM. Statistical test used is Two-way ANOVA with Tukey correction; ns = non-
1416 significant; * = p< 0.05.
1417 **(M)** Representative HE staining, and corresponding quantification of the average number of central
1418 nuclei of TA muscles of control Sham-operated or DHT-supplemented old male mice, 7 dpi. Cyan blue
1419 arrows point to immune infiltration. Black arrows denote central nuclei. White arrows show central
1420 or parallel nuclei alignments. Scale bars, 150 µm for transverse, and 100 µm for longitudinal sections.
1421 Data are presented as mean ± SEM. Statistical test used was two-tailed Mann-Whitney test; * = p <
1422 0.05.
1423 **(N-Q)** Representative immunofluorescent detections of PAX7 (green) **(N)**, PAX7 (green) and KI67
1424 (magenta) **(O)**, MYOG (red) **(P)**, and F4/80 (green) **(Q)**, and corresponding quantifications per field of
1425 injury in TA muscles of control Sham-operated or DHT-supplemented old male mice, 7 dpi. Nuclei were
1426 stained with DAPI. Scale bars, 50 µm (N), 20 µm (O), 20 µm (P), and 50 µm (Q). Data are presented as
1427 mean ± SEM. Statistical test used was two-tailed Mann-Whitney test; ns, non-significant.
1428
1429 **Figure 7: Androgen receptor governs MuSC function in aged muscle through mechanisms that differ**
1430 **from those operating in the young.**
1431 **(A-B)** Heatmap depicting the mean centered normalized expression of down- and upregulated genes
1432 from SMART-seq analysis performed on control MuSC FACS-isolated from 7-day-injured TA of old and
1433 young mice **(A)**, and corresponding gene ontology enrichment **(B)**.
1434 **(C)** Violin plots representing the normalized read counts of the indicated genes, selected from SMART-
1435 seq analysis performed control MuSC FACS-isolated from 7-day-injured TA of old and young mice.
1436 Statistical test used is Wald test; * = p < 0.05; ** = p < 0.01; *** = p < 0.001.
1437 **(D)** Venn diagrams showing intersected genes among differentially expressed genes in MuSC of control
1438 old mice and $AR^{(i)sat-/Y}$ young mice.
1439 **(E-F)** Cumulative number of down-regulated genes **(E)**, and up-regulated genes **(F)** in MuSC of 7-day-
1440 injured TA of old male mice, with an AR peak located at the indicated distances from their TSS.

1441 **(G)** Venn diagrams showing intersected genes with AR peaks among differentially expressed genes in
1442 MuSC of control old mice and $AR^{(i)sat-/Y}$ young mice.
1443 **(H)** Relative *AR* transcript levels in control LHCN-M2 and C79 myoblasts. Data are presented as mean
1444 ± SEM. Statistical test used was two-tailed Mann-Whitney test; ** = $p < 0.01$.
1445 **(I-J)** Representative western blot analysis **(I)**, and corresponding quantification of the indicated
1446 proteins **(J)** in control LHCN-M2 and C79 myoblasts. α-TUBULIN (TUB) was used as a loading control.
1447 Data are presented as mean ± SEM. Statistical test used was two-tailed Mann-Whitney test; * = $p <$
1448 0.05.
1449 **(K)** Representative immunofluorescent detection of PAX7 (in green) and AR (in red), in LHCN-M2 and
1450 C79 cells. Scale bars, 100 µm for the main, 10 µm for magnified inset.
1451 **(L)** Quantification of the percentage of high- and low/non-proliferative control LHCN-M2 and C79
1452 myoblasts as determined by CellTrace analysis. Data are presented as mean ± SEM. Statistical test
1453 used is Two-way ANOVA with Tukey correction; *** = $p< 0.001$.
1454 **(M)** Representative brightfield images of control (CTR), AR-siRNA transfected (siRNA-hAR) and AR-
1455 plasmid transfected (OE-hAR) LHCN-M2 and C79 cells, 0, 3- and 5-days post-differentiation (dpd).
1456 Black arrows show fibroblast-like non-differentiated cells. Red arrows label spindle-like differentiated
1457 cells. Scale bars, 100 µm.

FIGURE 1

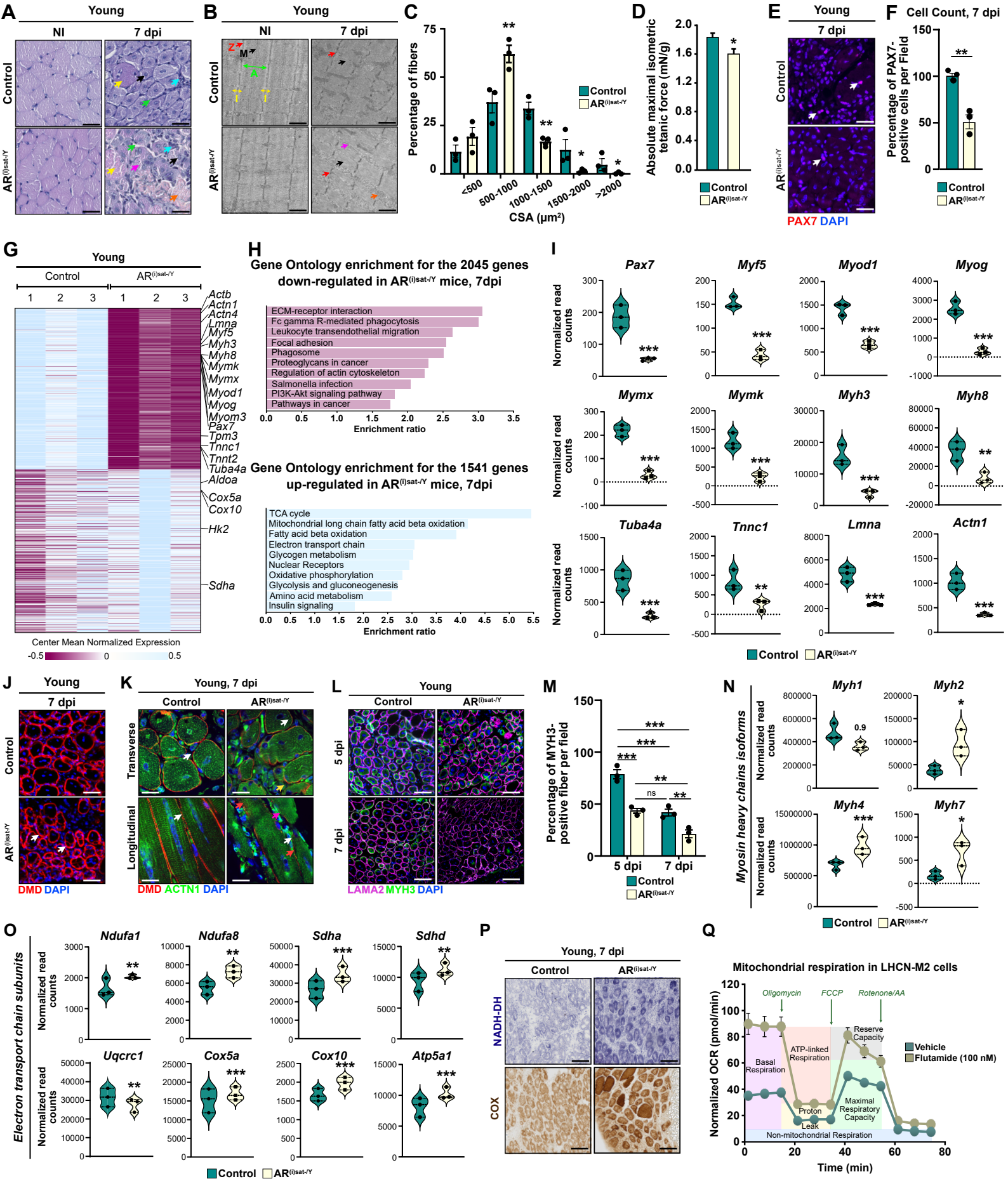
A
Young
NI
7 dpi
Control
AR(i)sat-/Y
B
Young
NI
7 dpi
Control
AR(i)sat-/Y
Z
M
A
I
C
Percentage of fibers
Control
AR(i)sat-/Y
<500
500-1000
1000-1500
1500-2000
>2000
CSA (µm²)
D
Absolute maximal isometric tetanic force (mN/g)
Control
AR(i)sat-/Y
E
Young
7 dpi
Control
AR(i)sat-/Y
PAX7 DAPI
F
Cell Count, 7 dpi
Percentage of PAX7-positive cells per Field
Control
AR(i)sat-/Y
G
Young
Control
AR(i)sat-/Y
Actb
Actn1
Actn4
Lmna
Myf5
Myh3
Myh8
Mymk
Mymx
Myod1
Myog
Myom3
Pax7
Tpm3
Tnnc1
Tnnt2
Tuba4a
Aldoa
Cox5a
Cox10
Hk2
Sdha
Center Mean Normalized Expression
H
Gene Ontology enrichment for the 2045 genes down-regulated in AR(i)sat-/Y mice, 7dpi
ECM-receptor interaction
Fc gamma R-mediated phagocytosis
Leukocyte transendothelial migration
Focal adhesion
Phagosome
Proteoglycans in cancer
Regulation of actin cytoskeleton
Salmonella infection
PI3K-Akt signaling pathway
Pathways in cancer
Enrichment ratio
Gene Ontology enrichment for the 1541 genes up-regulated in AR(i)sat-/Y mice, 7dpi
TCA cycle
Mitochondrial long chain fatty acid beta oxidation
Fatty acid beta oxidation
Electron transport chain
Glycogen metabolism
Nuclear Receptors
Oxidative phosphorylation
Glycolysis and gluconeogenesis
Amino acid metabolism
Insulin signaling
Enrichment ratio
I
Pax7
Myf5
Myod1
Myog
Mymx
Mymk
Myh3
Myh8
Tuba4a
Tnnc1
Lmna
Actn1
Normalized read counts
Control
AR(i)sat-/Y
J
Young
7 dpi
Control
AR(i)sat-/Y
DMD DAPI
K
Young, 7 dpi
Control
AR(i)sat-/Y
Transverse
Longitudinal
DMD ACTN1 DAPI
L
Young
Control
AR(i)sat-/Y
5 dpi
7 dpi
LAMA2 MYH3 DAPI
M
Percentage of MYH3-positive fiber per field
5 dpi
7 dpi
ns
Control
AR(i)sat-/Y
N
Myosin heavy chains isoforms
Myh1
Myh2
Myh4
Myh7
Normalized read counts
Control
AR(i)sat-/Y
O
Electron transport chain subunits
Ndufa1
Ndufa8
Sdha
Sdhd
Uqcrc1
Cox5a
Cox10
Atp5a1
Normalized read counts
Control
AR(i)sat-/Y
P
Young, 7 dpi
Control
AR(i)sat-/Y
NADH-DH
COX
Q
Mitochondrial respiration in LHCN-M2 cells
Oligomycin
FCCP
Rotenone/AA
Basal Respiration
ATP-linked Respiration
Proton Leak
Reserve Capacity
Maximal Respiratory Capacity
Non-mitochondrial Respiration
Normalized OCR (pmol/min)
Time (min)
Vehicle
Flutamide (100 nM)

FIGURE 2

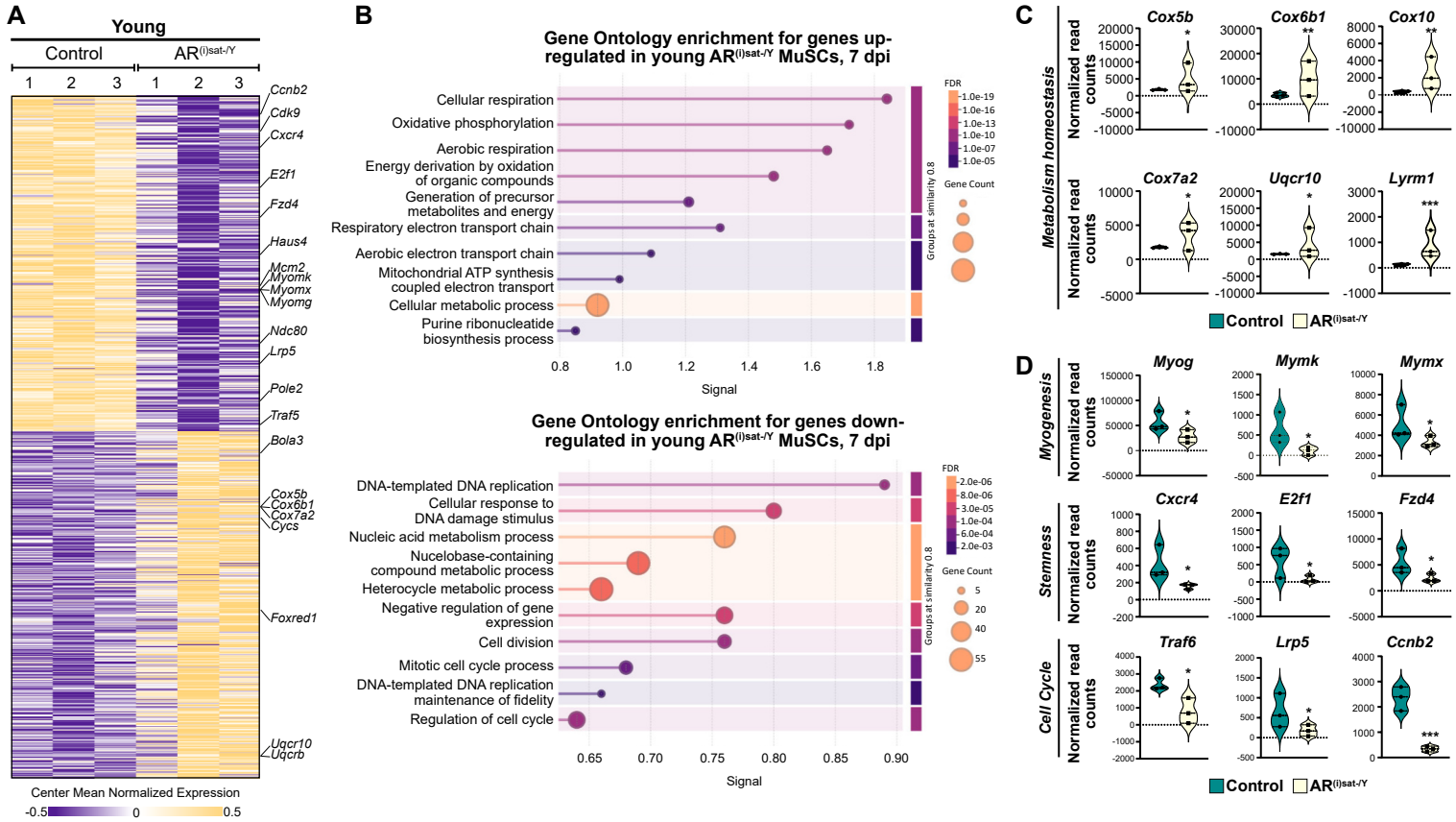

E

AR Known Motif Search

Name	Logo	p-value	% of Targets
ARE		1e-124	49.45 %
AR-half site		1e-17	68.13%

AR *de novo* Motif Search

Name	Logo	p-value	% of Targets
AR		1e-348	47.15 %
AR-half site		1e-13	8.79%

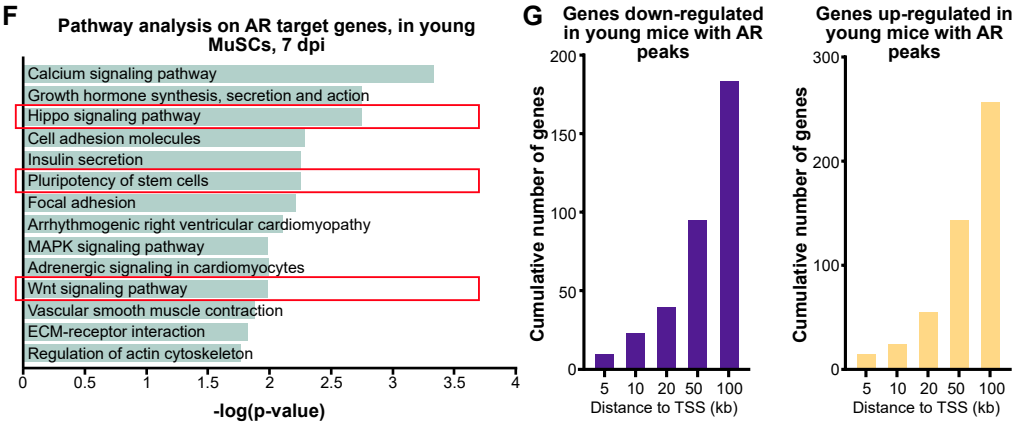

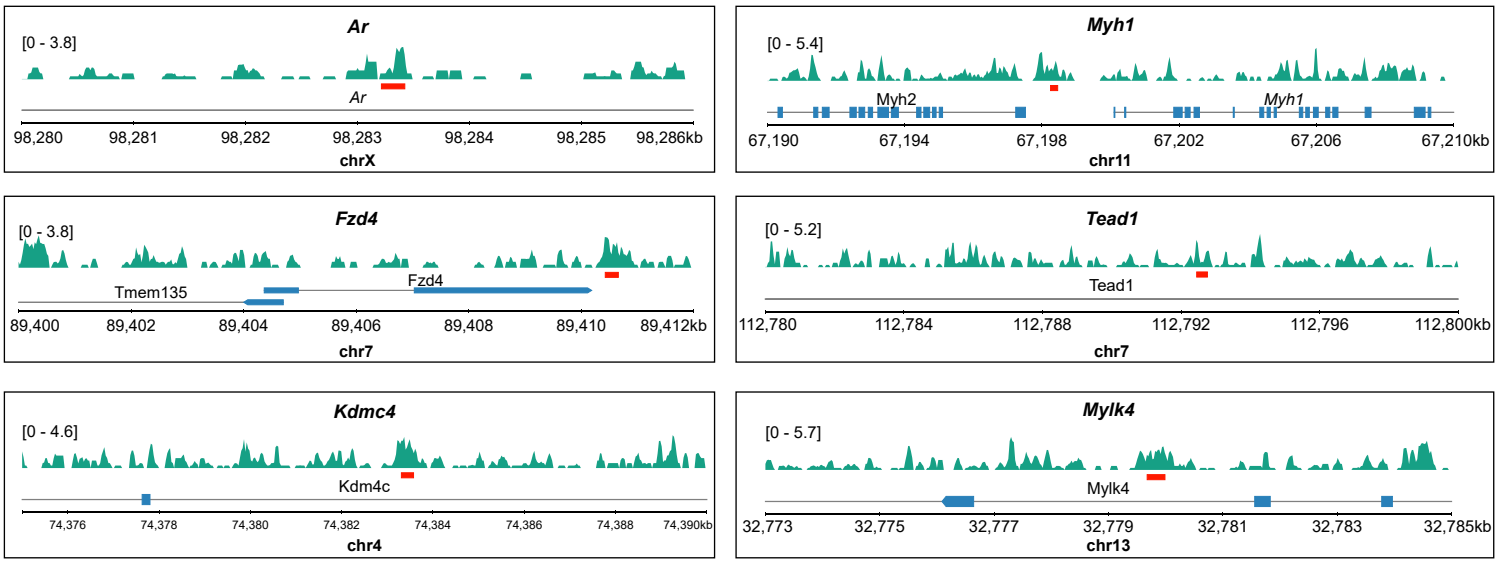

FIGURE 3

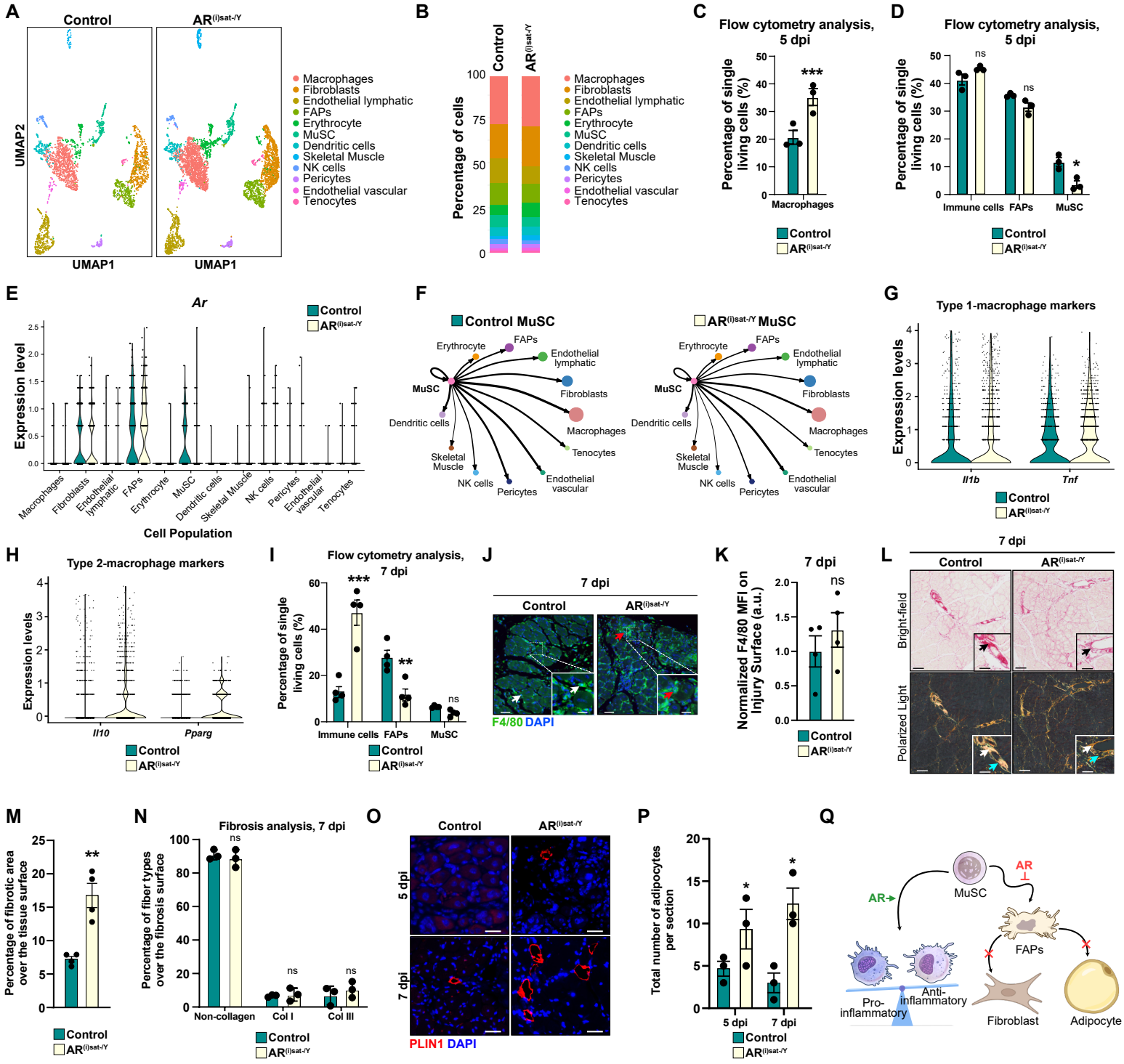
A
Control
AR(i)sat-/Y
UMAP2
UMAP1
UMAP1
Macrophages
Fibroblasts
Endothelial lymphatic
FAPs
Erythrocyte
MuSC
Dendritic cells
Skeletal Muscle
NK cells
Pericytes
Endothelial vascular
Tenocytes
B
Control
AR(i)sat-/Y
Percentage of cells
100
75
50
25
0
C
Flow cytometry analysis, 5 dpi
Percentage of single living cells (%)
***
Macrophages
Control
AR(i)sat-/Y
D
Flow cytometry analysis, 5 dpi
Percentage of single living cells (%)
ns
ns
*
Immune cells
FAPs
MuSC
Control
AR(i)sat-/Y
E
Ar
Control
AR(i)sat-/Y
Expression level
Cell Population
F
Control MuSC
AR(i)sat-/Y MuSC
Erythrocyte
FAPs
Endothelial lymphatic
MuSC
Fibroblasts
Dendritic cells
Macrophages
Tenocytes
Skeletal Muscle
NK cells
Pericytes
Endothelial vascular
G
Type 1-macrophage markers
Expression levels
Il1b
Tnf
Control
AR(i)sat-/Y
H
Type 2-macrophage markers
Expression levels
Il10
Pparg
Control
AR(i)sat-/Y
I
Flow cytometry analysis, 7 dpi
Percentage of single living cells (%)
***
**
ns
Immune cells
FAPs
MuSC
Control
AR(i)sat-/Y
J
7 dpi
Control
AR(i)sat-/Y
F4/80 DAPI
K
7 dpi
Normalized F4/80 MFI on Injury Surface (a.u.)
ns
Control
AR(i)sat-/Y
L
7 dpi
Control
AR(i)sat-/Y
Bright-field
Polarized Light
M
Percentage of fibrotic area over the tissue surface
**
Control
AR(i)sat-/Y
N
Fibrosis analysis, 7 dpi
Percentage of fiber types over the fibrosis surface
ns
ns
ns
Non-collagen
Col I
Col III
Control
AR(i)sat-/Y
O
Control
AR(i)sat-/Y
5 dpi
7 dpi
PLIN1 DAPI
P
Total number of adipocytes per section
*
*
5 dpi
7 dpi
Control
AR(i)sat-/Y
Q
AR
MuSC
AR
FAPs
Pro-inflammatory
Anti-inflammatory
Fibroblast
Adipocyte

FIGURE 4

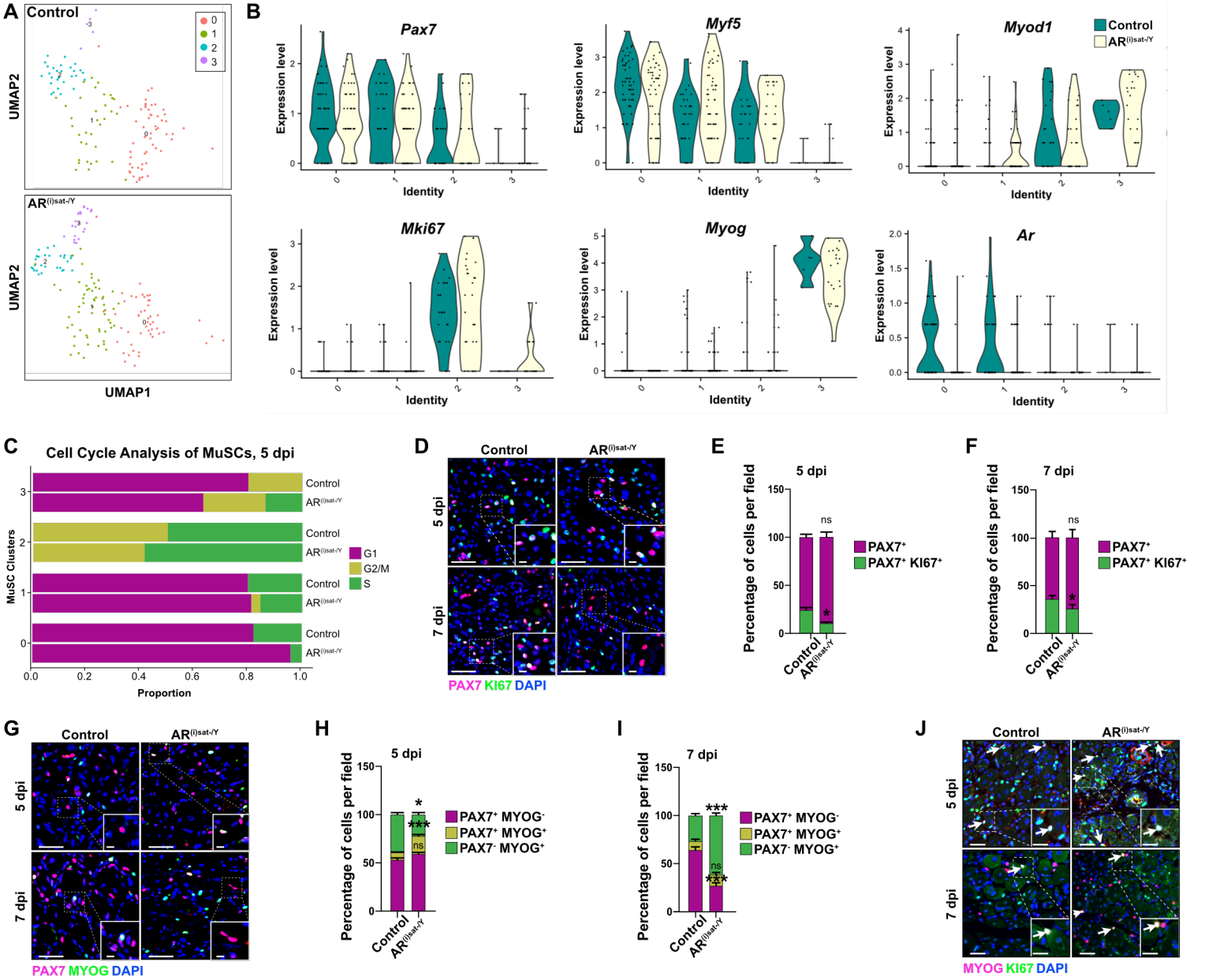
A
Control
AR(i)sat-/Y
UMAP2
UMAP1
B
Pax7
Myf5
Myod1
Mki67
Myog
Ar
Expression level
Identity
Control
AR(i)sat-/Y
C
Cell Cycle Analysis of MuSCs, 5 dpi
MuSC Clusters
Proportion
G1
G2/M
S
D
Control
AR(i)sat-/Y
5 dpi
7 dpi
PAX7 KI67 DAPI
E
5 dpi
Percentage of cells per field
PAX7+
PAX7+ KI67+
ns
F
7 dpi
G
PAX7 MYOG DAPI
H
PAX7+ MYOG-
PAX7+ MYOG+
PAX7- MYOG+
I
J
MYOG KI67 DAPI
K
Number of MYOG/MKI67-positive cells per field
L
Young
M
DMD PAX7 DAPI
N
28+7 dpi
Number of PAX7-positive cells per field
O
MuSC
AR
Maintenance plane
Commitment plane

FIGURE 5

A

AR Known Motif Search

Name	Logo	p-value	% of Targets
ARE		1e-55	26.2 %
AR-half site		1e-68	39.5%

AR *de novo* Motif Search

Name	Logo	p-value	% of Targets
AR		1e-348	47.15 %

B

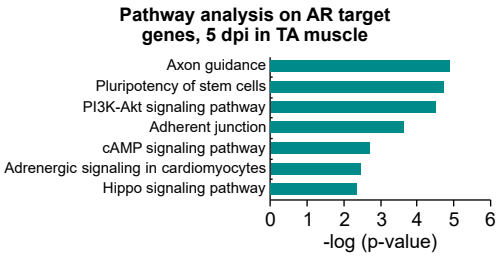

C

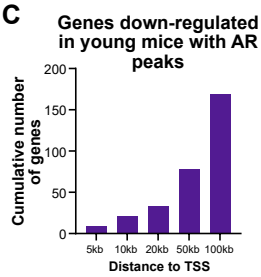

D

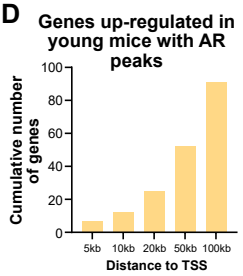

E

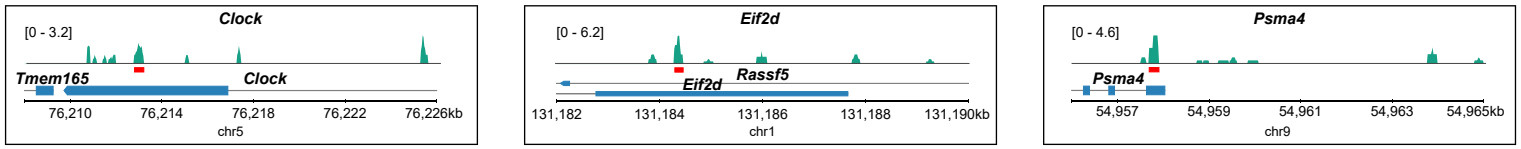

F

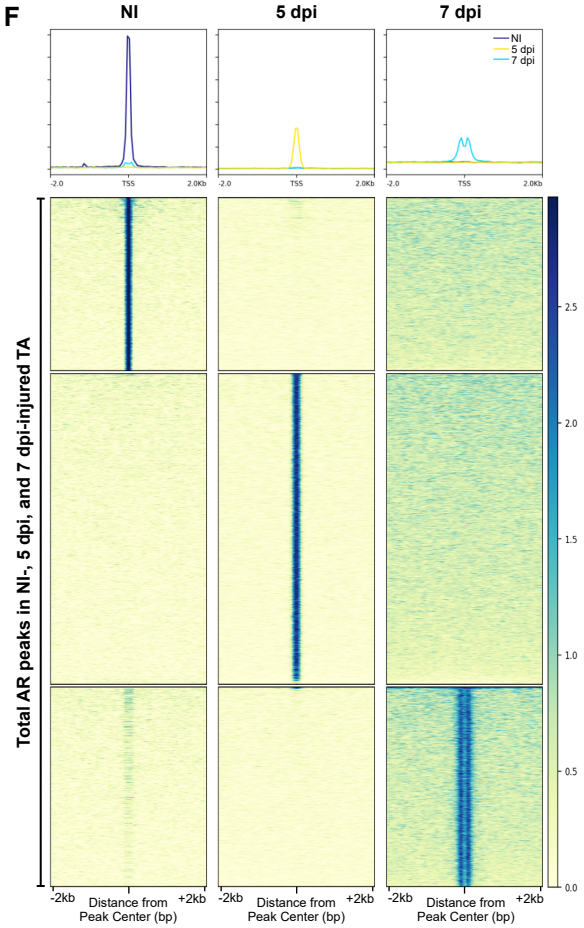

G

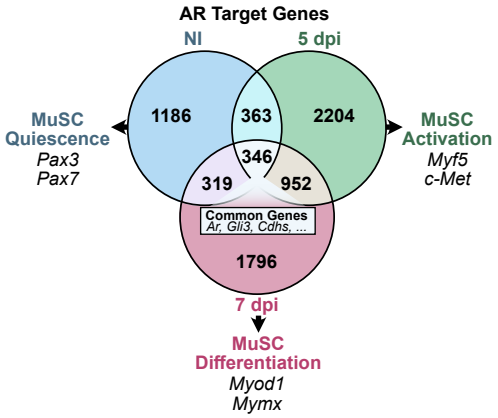

H

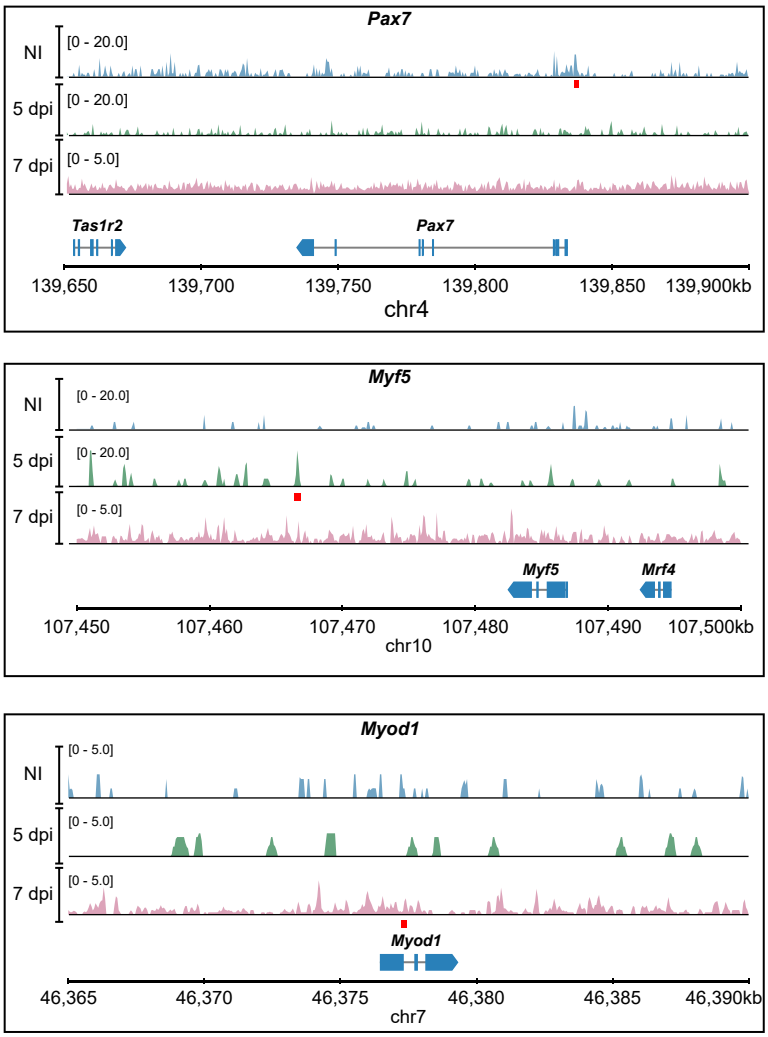

I

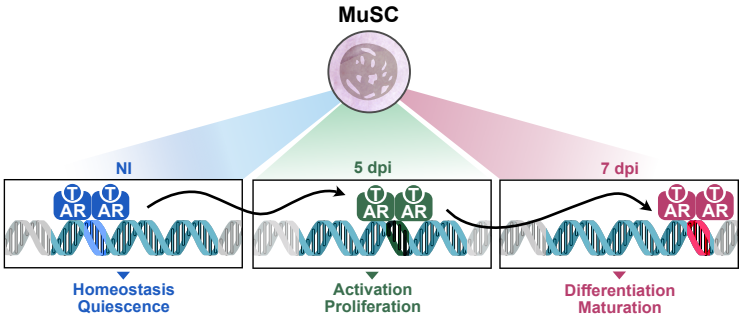

FIGURE 6

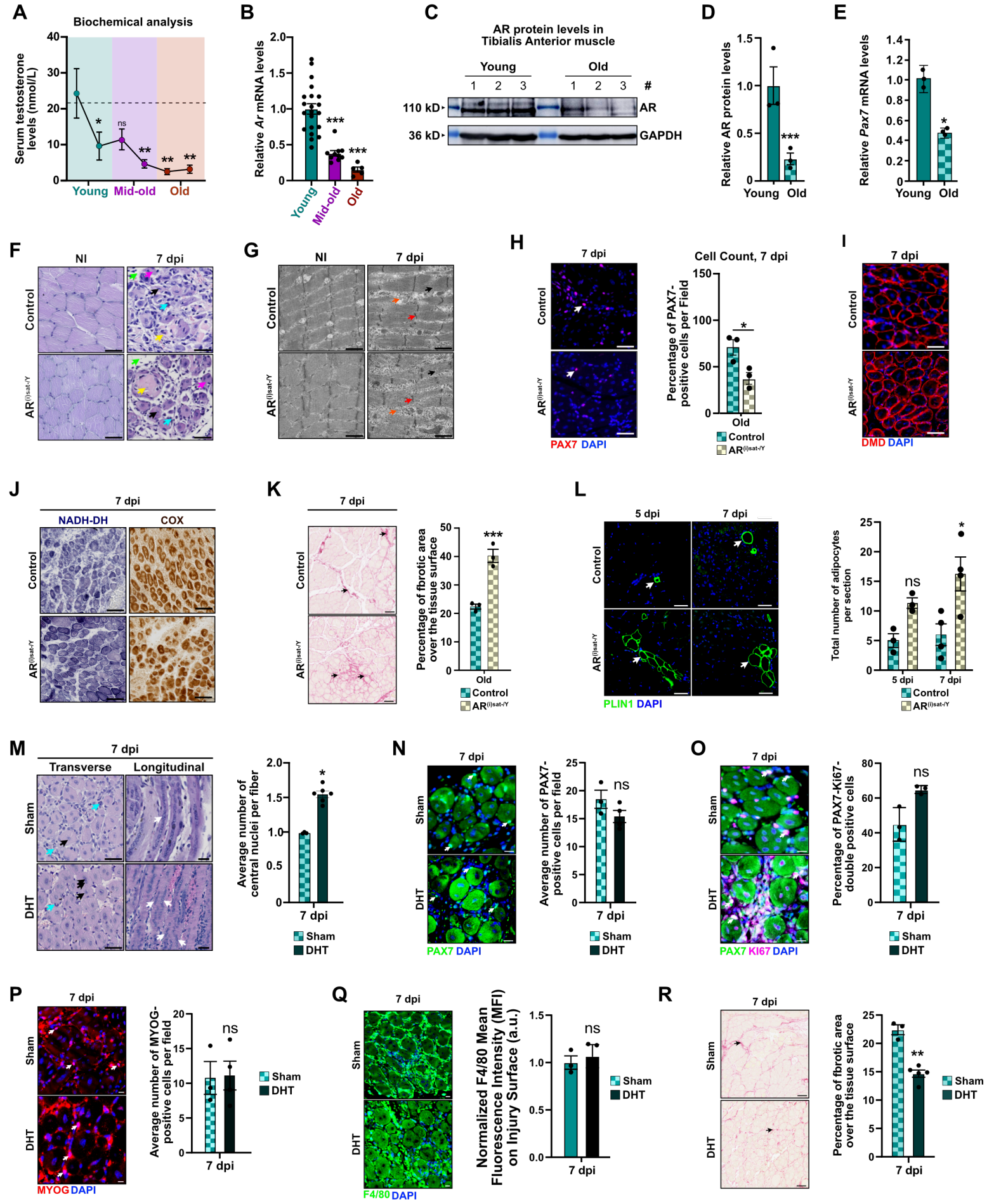
A
Biochemical analysis
Serum testosterone levels (nmol/L)
Young
Mid-old
Old
B
Relative Ar mRNA levels
C
AR protein levels in Tibialis Anterior muscle
Young
Old
110 kD
36 kD
AR
GAPDH
D
Relative AR protein levels
E
Relative Pax7 mRNA levels
F
NI
7 dpi
Control
G
H
7 dpi
Cell Count, 7 dpi
Percentage of PAX7-positive cells per Field
PAX7 DAPI
I
DMD DAPI
J
NADH-DH
COX
K
Percentage of fibrotic area over the tissue surface
L
5 dpi
PLIN1 DAPI
Total number of adipocytes per section
M
Transverse
Longitudinal
Sham
DHT
Average number of central nuclei per fiber
N
Average number of PAX7-positive cells per field
O
PAX7 KI67 DAPI
Percentage of PAX7-Ki67-double positive cells
P
MYOG DAPI
Average number of MYOG-positive cells per field
Q
F4/80 DAPI
Normalized F4/80 Mean Fluorescence Intensity (MFI) on Injury Surface (a.u.)
R
ns

FIGURE 7

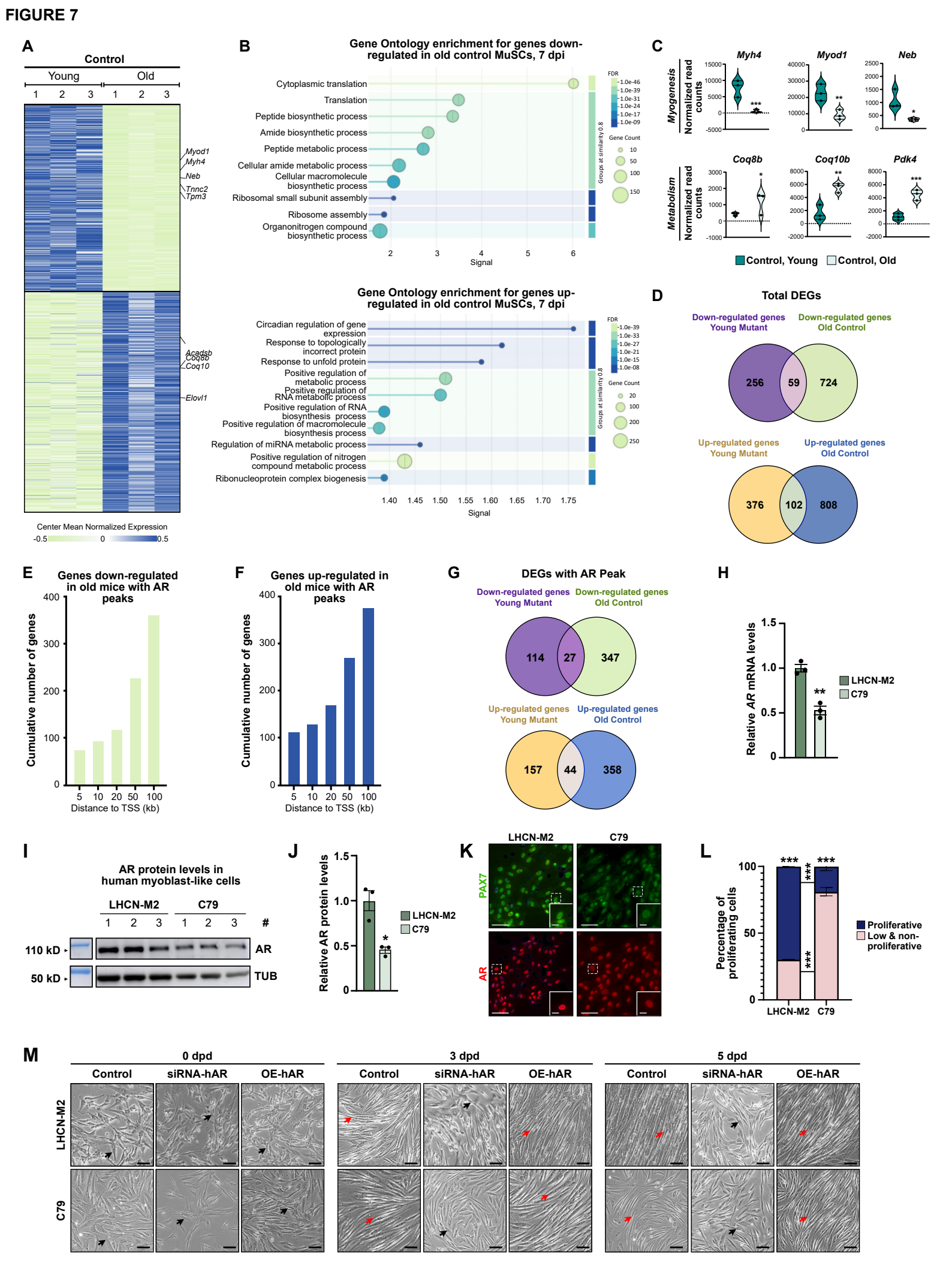
A
Control
Young
Old
1 2 3 1 2 3
Myod1
Myh4
Neb
Tnnc2
Tpm3
Acadsb
Coq8b
Coq10
Elovl1
Center Mean Normalized Expression
-0.5 0 0.5
B
Gene Ontology enrichment for genes down-regulated in old control MuSCs, 7 dpi
Cytoplasmic translation
Translation
Peptide biosynthetic process
Amide biosynthetic process
Peptide metabolic process
Cellular amide metabolic process
Cellular macromolecule biosynthetic process
Ribosomal small subunit assembly
Ribosome assembly
Organonitrogen compound biosynthetic process
Signal
FDR
Gene Count
Groups at similarity 0.8
Gene Ontology enrichment for genes up-regulated in old control MuSCs, 7 dpi
Circadian regulation of gene expression
Response to topologically incorrect protein
Response to unfold protein
Positive regulation of metabolic process
Positive regulation of RNA metabolic process
Positive regulation of RNA biosynthesis process
Positive regulation of macromolecule biosynthesis process
Regulation of miRNA metabolic process
Positive regulation of nitrogen compound metabolic process
Ribonucleoprotein complex biogenesis
C
Myogenesis
Metabolism
Normalized read counts
Myh4
Myod1
Neb
Coq8b
Coq10b
Pdk4
Control, Young
Control, Old
D
Total DEGs
Down-regulated genes Young Mutant
Down-regulated genes Old Control
256 59 724
Up-regulated genes Young Mutant
Up-regulated genes Old Control
376 102 808
E
Genes down-regulated in old mice with AR peaks
Cumulative number of genes
Distance to TSS (kb)
F
Genes up-regulated in old mice with AR peaks
Cumulative number of genes
Distance to TSS (kb)
G
DEGs with AR Peak
Down-regulated genes Young Mutant
Down-regulated genes Old Control
114 27 347
Up-regulated genes Young Mutant
Up-regulated genes Old Control
157 44 358
H
Relative AR mRNA levels
LHCN-M2
C79
I
AR protein levels in human myoblast-like cells
LHCN-M2
C79
110 kD
50 kD
AR
TUB
J
Relative AR protein levels
LHCN-M2
C79
K
LHCN-M2
C79
PAX7
AR
L
Percentage of proliferating cells
Proliferative
Low & non-proliferative
LHCN-M2
C79
M
0 dpd
3 dpd
5 dpd
Control
siRNA-hAR
OE-hAR
LHCN-M2
C79